Analysis of Damage Mechanisms in Boronized TZM Tiles from Alcator C-Mod Fusion Reactor Operations

by

Joseph Michael Hubley

Submitted to the Department of Nuclear Science and Engineering
in partial fulfillment of the requirements for the degree of
Master of Science in Nuclear Science and Engineering
at the
MASSACHUSETTS INSTITUTE OF TECHNOLOGY
June 2010

MASSACHUSETTS INSTITUTE OF TECHNOLOGY
DEC 0 9 2010
LIBRARIES

© Massachusetts Institute of Technology 2010. All rights reserved.

ARCHIVES

Author .....
Department of Nuclear Science and Engineering
May 14, 2010

Certified by .....
Ronald G. Ballinger
Professor of Nuclear Science and Engineering
Thesis Supervisor

Certified by .....
Dennis G. Whyte
Associate Professor of Nuclear Science and Engineering
Thesis Supervisor

Certified by .....
Bruce Lipschultz
Senior Research Scientist
Thesis Supervisor

Accepted by .....
Professor Jacqueline C. Yanch
Chair, Department Committee on Graduate Students

Analysis of Damage Mechanisms in Boronized TZM Tiles from Alcator C-Mod Fusion Reactor Operations

by

Joseph Michael Hubley

Submitted to the Department of Nuclear Science and Engineering
on May 14, 2010, in partial fulfillment of the
requirements for the degree of
Master of Science in Nuclear Science and Engineering

Abstract

Alcator C-Mod is a deuterium tokamak reactor experiment operated by the MIT Plasma Science and Fusion Center. Following the 2008 Alcator C-Mod campaign, the reactor was shut down and opened for maintenance and upgrades. During this time, it was discovered that the boronized TZM tiles, with boron films applied in situ, lining the inner surfaces of the reactor had experienced non-uniform damage as a result of plasma interactions. This damage was most pronounced in the tiles from the limiter and divertor, but also appeared in regions of the reactor that were not traditionally believed to experience high heat or particle fluxes. The objective of this thesis is to perform a thorough microstructural analysis of these tiles, particularly the boron-TZM interface, in order to explore the damage mechanisms present. In turn, the details of the damage mechanisms will illuminate the plasma parameters, such as temperature and particle flux, that caused the damage. This analysis will also allow for a prediction of the behavior of other tile and coating materials under consideration for use in fusion devices.

During this investigation, a number of tiles with varying degrees of apparent damage were removed from the limiter and divertor and photographed for macroscopic characterization. Modeling was also performed using the expected heat and particle fluxes at the tile surface, along with the thermal transient history of the tiles, to estimate the depth of damage from each of these sources. These results were compared to data gathered during analysis of the tiles through several techniques, including ion beam analysis, scanning electron and optical microscopy, energy dispersive X-ray spectroscopy, and X-ray diffraction spectroscopy.

Ultimately, the diverse sets of data gathered through these techniques provided for a fairly cohesive rationalization of the damage mechanisms present. In the case of the divertor tiles, no thermal damage was observed, but the boron film was eroded through sputtering as a result of the large fluxes of high energy particles encountered in that region of the reactor. Tiles in the limiter, however, experienced a more severe amount of damage caused primarily by thermal effects. The surface temperatures at these tiles were in the range 2140-2600 degrees Celsius, surpassing the melting point

of boron and approaching that of the underlying TZM. Recrystallization of the TZM substrate was observed to an average depth of ~20μm, with an overall observed heat penetration depth of ~100μm. These temperatures indicate a local heat flux of ~10^8-10^9W/m^2 when applied to the heat diffusion model used earlier in this investigation.

Such a large heat flux indicates a transient event responsible for the observed damage, occurring on a timescale of milliseconds rather than the one second duration of a pulse at peak power. This transient would be characterized by an increase by an order of magnitude of the product of the plasma density and sheath temperature. Another possibility is that the beads which formed on the melted surface extended beyond the plasma Debye length and intersected the magnetic field lines, resulting in an increase in the heat fluxy by an order of magnitude at those locations. It is difficult to separate the contributions of these damage mechanisms from data obtained after a full Alcator campaign, and further investigation is warranted to better understand each of these processes.

Thesis Supervisor: Ronald G. Ballinger
Title: Professor of Nuclear Science and Engineering

Thesis Supervisor: Dennis G. Whyte
Title: Associate Professor of Nuclear Science and Engineering

Thesis Supervisor: Bruce Lipschultz
Title: Senior Research Scientist

Acknowledgments

I would like to thank the many people who supported my work on this thesis for their contributions.

Ron Ballinger, Dennis Whyte, and Bruce Lipschultz, for their direction and guidance throughout this investigation.

Harold Barnard, for all of his contributions at the accelerator lab.

Julian Benz, Mike Short, Jon Gibbs, and Tim Lucas, for their advice on sample preparation and microstructural analysis.

Bob Mumgaard, Dan Brunner, Geoff Olynyk, Mike Garrett, and Zach Hartwig, for their detailed knowledge of Alcator C-Mod.

Contents

1 Introduction **17**

1.1 Overview of Fusion Energy 18

1.2 Tokamak Reactors 20

1.3 Alcator C-Mod 21

1.4 Motivation for Thesis 24

2 Theoretical Background **25**

2.1 Recrystallization 25

2.2 Intermetallic Phase Precipitation 29

2.3 Estimated Transient Temperature 30

2.4 Ion Beam Analysis (IBA) 30

2.4.1 Particle Induced Gamma Emission (PIGE) 31

2.4.2 Rutherford Back Scattering (RBS) 32

2.5 Scanning Electron Microscopy (SEM) 34

2.6 Energy Dispersive X-Ray Spectroscopy (EDX) 35

2.7 X-Ray Diffraction (XRD) 35

2.8 Determination of Plasma Properties 37

3 Materials and Methods **41**

3.1 Tile Selection and Macroscopic Characterization 41

3.2 Modeling 42

3.2.1 Thermal Damage 47

3.2.2 Radiation Damage 48

3.3 Ion Beam Analysis 49
3.3.1 Particle Induced Gamma Emission 50
3.3.2 Rutherford Back Scattering 52
3.4 Microstructural Characterization 53
3.5 X-Ray Diffraction 55

4 Results **57**
4.1 Ion Beam Analysis 57
4.1.1 PIGE Results 57
4.1.2 RBS Spectra 57
4.1.3 Integration of IBA Results 60
4.2 Microstructural Analysis 61
4.2.1 Optical Micrographs 61
4.2.2 SEM Micrographs 64
4.3 XRD Spectra 65
4.4 Summary of Tile Data 69

5 Discussion **73**

6 Conclusions **79**

List of Figures

1-1 The toroidal and poloidal fields produced by a tokamak reactor for plasma confinement. 20

1-2 Schematic of Alcator's bare vacuum vessel. 22

1-3 Schematic of the poloidal cross-section of Alcator C-Mod, with the limiter and divertor indicated. The red line separates open and closed magnetic field lines. 23

2-1 Recrystallization temperature as a function of cold work, represented by percent reduction in bar thickness during rolling, for several molybdenum alloys. These data represent the onset of recrystallization, following nucleation, for a one hour isothermal anneal. The behavior of TZM is given by the uppermost curve. 26

2-2 The degree of recrystallization versus temperature for a one hour duration of heating for molybdenum (blue), TZM (red), and tungsten (green). Note that the degree of recrystallization for all three alloys increases dramatically over a relatively small range of temperatures. . 27

2-3 Recrystallization temperature of TZM as a function of the duration of isothermal heating, with the temperature representing the onset of recrystallization, following nucleation. The red curve is the upper temperature bound and the blue curve is the lower temperature bound for the range of recrystallization temperatures. 28

2-4 Boron-molybdenum phase diagram, indicating the compositions and temperatures at which several common intermediate B-Mo phases are stable. Such phases may be formed as precipitates by boron diffusion into the underlying molybdenum of the tiles at high temperature. . . 29

2-5 Cross section for proton-induced emission of the 432keV gamma ray by ^{10}B. Note the sharply peaked resonance that occurs at 1.5MeV. . . 32

3-1 The poloidal locations of the damaged Alcator tiles (1) A41171I and A41258I, (2) G20, (3) G15S, (4) G13S, and (5) G7. 43

3-2 The poloidal location of the undamaged tile 070B40809R, indicated in the top right corner of the schematic. 43

3-3 A map of the GH limiter, showing the locations of tiles G7, G13S, G15S, and G20. 44

3-4 A photo of the GH limiter, showing the tiles along the left and right edges recessed in major radius. 45

3-5 A radial view of G15S, a tile from the left edge of the GH limiter module. The magnetic field lines are parallel to the flat plasma facing surface on the side of the tile nearer the center of the limiter, with the rounded side nearer the edge of the limiter receding away from the plasma. 45

3-6 Macrophotographs of the damaged surfaces of tiles used in this investigation. 46

3-7 Thermal conductivity of TZM versus temperature. 47

3-8 The 1.7MV Tandetron accelerator at the CLASS facility. 49

3-9 Schematic of the Tandetron accelerator, indicating the locations of the (1) ion source, (2) low energy steering magnet for ion selection, (3) path of negative ion acceleration, (4) high voltage terminal with electron stripping occurring in nitrogen gas, (5) path of positive ion acceleration, (6) quadrupole focusing magnet, and (7) high energy steering magnet. 50

3-10 Photographs of the entire tile surface for tiles used in IBA. All tile surface locations are referenced to these photographs. For the limiter tiles G7, G13S, and G15S, the right hand side in these photographs is the rounded edge of the tile which would be at the edge of the GH limiter, as shown in the radial view of G15S provided in Figure 3-11. Note that the limiter tiles in these photographs are in opposite orientation to their installed location, as shown in Figure 3-11. 51

3-11 A radial view of G15S, a tile from the left edge of the GH limiter module. The magnetic field lines are parallel to the flat plasma facing surface on side of the tile nearer to the center of the limiter, with the rounded side at the edge of the limiter receding away from the plasma. Note that the orientation of the tile in this view is equivalent to that when installed in the limiter module, but opposite the orientation of the limiter tile photographs shown in Figure 3-10. 52

3-12 Schematic of the cutting surfaces for different tile geometries. For the microstructural analysis, sections 2 and 3 are viewed along cutting surface 1, and sections 1 and 4 are viewed along cutting surface 2. The section numbers above also correspond to the damaged tile surfaces shown in Figure 3-10, with section 1 from the top left quadrant, 2 from the top right, 3 from the bottom left, and 4 from the bottom right. 53

4-1 RBS spectra obtained with five of the damaged tiles, each shown against the spectrum obtained with a bare Mo tile. 59

4-2 The microstructure of the undamaged TZM substrate, as viewed in a plane parallel to a side of the tile ~1mm below the boronized surface. This microstructure is dominated by elongated grains, ~20μm in width and oriented along the direction of rolling during fabrication. 61

4-3 A recrystallized grain, ~10μm wide, found at the boron-TZM interface in section 3 of tile G13S. 62

4-4 A large recrystallized grain found in section 4 of tile G13S. Note that the grain diverges from the orientation of grains in the substrate, instead wrapping around the surface defect. The width of this grain varies from ~10μm on one side of the defect to ~30μm on the opposite side. 63

4-5 An optical micrograph of section 4 of tile A41258I, showing the relatively intact boron film. 64

4-6 SEM micrograph of the undamaged TZM substrate along a grain boundary, showing a plane parallel to a side of the tile and approximately 100μm below the film. Note the dark pits along this boundary, which were most likely the location of Ti or Zr precipitates. 65

4-7 SEM micrograph of the boron-TZM interface from section 2 of tile G13S, approximately 100μm below the film. Note the light spots which indicate precipitates along the grain boundaries, possibly in the form of B-Mo phases. 66

4-8 Comprehensive XRD spectra for G7 and G15S obtained with the Panalytical X-ray diffractometer, with G7 shown in green and G15S in black. The numbered lines indicate the relative intensities and 2θ values of commonly observed XRD peaks for Mo, B, and several intermediate phases. 67

4-9 High resolution XRD spectra for G7 and G15S obtained with the Bruker D8 two-dimensional X-ray diffractometer, with G7 shown in green and G15S in black. The numbered lines indicate the relative intensities and 2θ values of commonly observed XRD peaks for Mo, B, and several intermediate phases. 68

4-10 Panalytical XRD spectra for a section of undamaged tile, G7, and G15S, shown in black, blue, and red, respectively. The common XRD peaks for B, Mo, and intermediate phases are given at the bottom, and the Mo K-β peaks are indicated in the spectra. 70

5-1 The temperature profiles throughout the limiter tiles anticipated by Equation 2.11 for a heat flux of $\sim 10^9 W/m^2$ and transient timescales of 1ms (blue), 0.9ms (red), and 0.8ms (green). 75
5-2 The beryllium-tungsten phase diagram. 77

List of Tables

3.1 List of tiles removed from Alcator C-Mod for analysis, along with their locations within the reactor during the 2008 campaign. 42

3.2 Estimated depths of thermal damage for both full pulse and transient timescales in tiles with given near surface concentrations of boron. . . 48

3.3 Four step polishing procedure for tile sections using Buehler products. 54

4.1 PIGE data collected at various locations on the damaged tiles. The locations given are referenced to the damaged surfaces of the tiles, as viewed with the tile orientation shown in Figure 3-10. The 432keV counts in each area were normalized by both incident protons and counts obtained from BN, then used with the simulation described earlier to determine the near surface ($\leq$30μm below the film) concentrations of boron. 58

4.2 The energy differences at the RBS edge between pure Mo and the damaged tiles, as well as the thickness of the B layer corresponding to such a difference, assuming a pure B film above the TZM substrate. 58

4.3 Comparison of near surface B concentrations as determined through both PIGE and RBS. 60

4.4 Summary of the tile data gathered through IBA, microscopy, and XRD techniques. 71

Chapter 1

Introduction

The use of nuclear fusion as a source of energy has been under investigation for decades. At the Massachusetts Institute of Technology (MIT), the Alcator C-Mod tokamak reactor is at the heart of research being conducted by the Plasma Science and Fusion Center (PSFC). Since 1992, this reactor has been in operation through a series of approximately yearlong campaigns. During such a campaign, plasmas containing the hydrogen isotope deuterium (D) are heated in $\sim$2.0s pulses to temperatures of $\sim 10^8$K, at which D-D fusion occurs. Although these plasma pulses are magnetically confined, interactions between the plasma and inner surface of the reactor do occur. To protect the reactor walls from damage during such interactions, the inner surface of Alcator is lined with a closely packed grid of boronized TZM tiles. Following the 2008 campaign, Alcator underwent scheduled maintenance that revealed unanticipated degradation of numerous tiles in the limiter and divertor regions of the reactor. The objective of this thesis is to characterize the damage mechanisms present in these tiles using a host of materials science techniques, then use this analysis to characterize the behavior of other tile and film materials, as well as to better understand the properties of the plasma itself.

1.1 Overview of Fusion Energy

As a field of research, nuclear fusion has been the subject of much excitement and controversy, not only today but throughout its brief half a century of existence. It originated somewhat ominously in a time of conflict, resulting in the development of the most destructive weapons known to mankind. Despite this bellicose inception, the fusion research being undertaken at present seeks a solution to one of the greatest global challenges of this century. As climate change and responsible energy management take increasing priority, nuclear fusion offers tremendous promise as a source of ecologically benign, abundant energy. The creation of a reactor capable of reliably and continuously providing such energy has been the focus of fusion research for several decades; however, numerous engineering challenges remain to be solved before such a reactor may become operational.

The attraction of nuclear fusion as a source of clean energy derives largely from the enormous energy density of the fuel. For instance, several MeV of useful energy may be obtained from the fusion of two deuterium atoms due to either the reaction

$$D + D \rightarrow^3 He + n + 3.27MeV, \tag{1.1}$$

or

$$D + D \rightarrow T + p + 4.03MeV, \tag{1.2}$$

where n is a free neutron, T is the hydrogen isotope tritium, and p is a free proton. An even more impressive 17.6 MeV per reaction may be obtained through the fusion of deuterium and tritium according to

$$D + T \rightarrow \alpha + n + 17.6MeV, \tag{1.3}$$

where α represents an alpha particle, or ^{4}He nucleus. These energy yields dwarf the $\sim$10eV of energy typically produced by a chemical reaction. Also, while fission reactions typically yield $\sim$200MeV, the masses of the isotopes involved are two orders

of magnitude greater than those fueling the fusion reactions above, and so fusion generally produces more energy per unit mass of fuel than fission [1].

In addition to its energy density, the fuel for fusion reactions is also naturally abundant and simple to procure. Although deuterium is far less common than single proton hydrogen, with one D atom for every 6700 atoms of ^{1}H, there is nonetheless enough deuterium in ocean water to satisfy the current global energy demand for two billion years. The tritium required for the reaction in Equation 1.3 is too short-lived to be found naturally on Earth; however, it may be bred by bombarding the common element lithium with neutrons, another product of fusion. It is also important to note that the products of fusion are either recyclable in the above reactions, or inert as is the case for helium. Secondary radioactivity may be produced from neutron activation of structural materials in the reactor, but the majority of these isotopes are short-lived and do not require storage on geological timescales, as does nuclear waste generated by fission reactors [1].

Unfortunately, the benefits of fusion energy are accompanied by several challenges. In order to initiate the reactions in Equations 2.7-1.3, the fuel must be brought to extreme temperatures, on the order of 10^8K. At such temperatures, the tendency of the fuel, now in a plasma state, is to expand due to kinetic pressure. This renders the fusion reactions unsustainable without some form of confinement. Also, in spite of the various confinement techniques used by present fusion reactors, particles do manage to escape from the confined plasma and interact with the inner surfaces of the reactor. These interactions rapidly cool the plasma and bring fusion to a halt, while also causing substantial degradation of the reactor's plasma facing components (PFCs). These and other issues must be overcome before fusion reactors can achieve steady state operation and become a reliable source of environmentally sound energy [1].

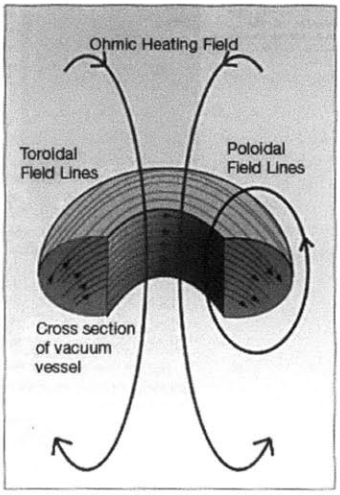

Figure 1-1: The toroidal and poloidal fields produced by a tokamak reactor for plasma confinement.
[2]

1.2 Tokamak Reactors

An important development in the quest to overcome the previously stated challenges of fusion energy is the invention of the tokamak reactor. Tokamak reactors are fusion devices that rely on powerful magnetic fields to confine the high temperature plasma described above. Tokamaks are toroidal in geometry, and they generate a magnetic field that is on the order of several Tesla for plasma confinement. To produce such a strong field, tokamaks rely on both external coils and a current driven directly through the plasma, producing a toroidal and poloidal magnetic field, respectively. The combination of both toroidal and poloidal fields is necessary to achieve stable confinement of the plasma. These fields are illustrated in Figure 1-1 [2]. Along with magnetic field generation, the plasma current contributes to the high temperatures necessary for fusion through ohmic heating of the plasma. This resistive heating alone is not enough to achieve the temperatures necessary for fusion, and so resonant radio frequency (RF) waves and high energy beams of neutral particles are used to further heat the plasma and induce fusion [3].

Thus far, tokamaks have been quite successful in fusion research relative to other reactors, particularly in regard to high temperature generation and plasma confine-

ment. Nonetheless, tokamaks are inherently pulsed devices, due to the finite flux sweep available for magnetic field production. Once the flux sweep is complete, the plasma current decays in short order due to resistive losses. At present, the duration of these plasma pulses is on the order of seconds. It is hoped that future tokamaks will be capable of pulses on the timescale of hours, with little time between pulses, so that near continuous operation may be achieved. Although current tokamaks will never produce commercially available energy, they serve a valuable function as research instruments for the development of fusion power [4].

1.3 Alcator C-Mod

Alcator C-Mod is a tokamak reactor, the third in a series of similar devices, currently being used for fusion research by the MIT PSFC. It has been in operation since 1992 through a series of approximately yearlong campaigns, each of which has been followed by a period of maintenance and upgrades. With a major radius of 0.67m and capable of generating a magnetic field up to 8T in strength, Alcator is a compact, high field tokamak. Deuterium plasmas are formed in Alcator in pulses of $\sim$2.0s, with typical densities of $<10^{20}$particles/m^3. Using RF heating, these plasmas can be heated to $\sim 10^8$K, a sufficient temperature for D-D fusion to occur. Figure 1-2 shows a schematic of Alcator's bare vacuum vessel.

Despite the strong magnetic fields used to contain the plasma, particles inevitably manage to escape and interact with the structure of the vacuum vessel. To mitigate the effects of these interactions, specific structures, namely the limiter and the divertor, have been incorporated into the design of Alcator. The limiter is a curved surface at the major radius of the vacuum vessel which directly intercepts the edge of the plasma. As ions at the edge of the plasma interact with the limiter, they transfer much of their energy and are neutralized. In this way, the limiter removes particles from the plasma edge and defines the shape of the plasma [6]. The limiter region is indicated in the schematic of the poloidal cross-section of Alcator C-Mod, shown in Figure 1-3 [7].

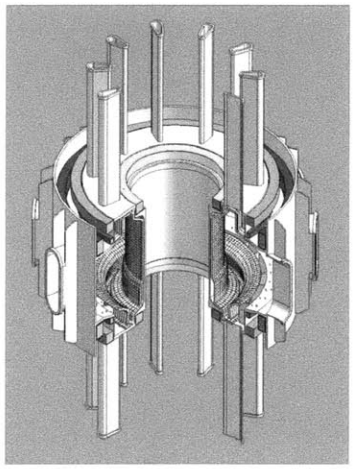

Figure 1-2: Schematic of Alcator's bare vacuum vessel.
[5]

The divertor in Alcator C-Mod is also shown in Figure 1-3 [7]. The primary purpose of the divertor is to remove particles from the edge of the plasma, neutralizing them as they collide at the divertor strike point and then allowing for the unconfined neutral particles to be pumped from the system. The divertor also allows tokamaks to benefit from an enhanced confinement regime, known as H-mode, which creates a steep pressure gradient at the plasma edge that almost doubles the energy confinement of the plasma. In terms of PFCs, the divertor aids in reducing thermal damage by increasing the wetted surface area of the plasma by using grazing incidence angles ($\sim$1-2^{o}) of magnetic fields to material surfaces. This produces a more evenly distributed heat flux, so that the temperature at the divertor surface is greatly reduced from that at the plasma edge [6].

As may be seen in Figures 1-2 and 1-3, the inner surface of the vacuum vessel is protected from the plasma by a closely packed grid of tiles. The majority of these tiles are composed of the molybdenum alloy TZM, although some tungsten tiles were also used in the 2008 campaign. TZM consists of a molybdenum matrix containing 0.4-0.55wt% titanium, 0.06-0.12wt% zirconium, and 0.01-0.03wt% carbon [8]. This alloy is commonly encountered in high temperature applications due to its high melting point of 2620^{o}C [9]. In general, molybdenum alloys maintain high strength and stability at higher temperatures, with performance rivaled only by tungsten alloys.

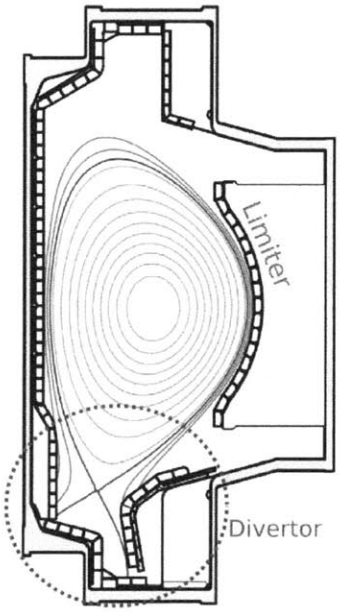

Figure 1-3: Schematic of the poloidal cross-section of Alcator C-Mod, with the limiter and divertor indicated. The red line separates open and closed magnetic field lines. [7]

Also, the high ductility and toughness of molybdenum alloys allow a greater tolerance for imperfections and reduced risk of brittle fracture over tungsten alloys and ceramics [10]. TZM is additionally favored in Alcator because it is less expensive and easier to machine than tungsten [11].

Although TZM is well suited to fusion applications because of its thermal properties, the Mo comprising the bulk of the alloy is high in atomic number (Z), as are the Ti and Zr. High Z elements must be prevented from entering the plasma, as their presence will cause rapid cooling through line radiation. To combat this high Z contamination, the tiles are all coated with a thin layer of boron using an in-situ low temperature plasma deposition. This is done with a helium diborane ($He+D_2B_6$) plasma that is RF heated at the electron cyclotron resonance frequency. This creates a resonance region, where boron is deposited, that may be swept across the inner surface of the reactor by varying the toroidal magnetic field. A typical campaign can distribute boron films $\sim$1-5μm thick on TZM surfaces [12].

1.4 Motivation for Thesis

Following the 2008 Alcator C-Mod campaign, the reactor was shut down and opened for maintenance and upgrades. During this time, it was discovered that the boronized TZM tiles had experienced non-uniform damage as a result of plasma interactions. This damage was most pronounced in the tiles from the limiter and divertor, but also appeared in regions of the reactor that were not traditionally believed to experience high heat or particle fluxes. The objective of this thesis is to perform a thorough microstructural analysis of these tiles, particularly the boron-TZM interface, in order to explore the damage mechanisms present. In turn, the details of the damage mechanisms will illuminate the plasma parameters, such as temperature and particle flux, that caused the damage. These damage mechanisms may also be extrapolated to predict the behavior of other tile and film materials under consideration for use in fusion devices. The results of this analysis will be useful not only for future selection of PFC materials, but also for improving the current understanding of plasma behavior inside Alcator and other tokamak reactors.

Chapter 2

Theoretical Background

Evidence of interactions between the plasma and PFCs, particularly the boronized TZM tiles in Alcator C-Mod, can manifest itself in a variety of forms. In the case of the boron film, contact with the plasma most often leads to erosion of the film through sputtering. Some of this sputtered boron may be redeposited on other tiles, so that boron will migrate throughout the reactor. Also, if the temperature at the tile surface exceeds 2075^{o}C, the boron will melt and redistribute itself along the tile surface [13]. The more likely scenario would be the deposition of sufficient energy to induce recrystallization and/or diffusion of boron from the surface into the TZM substrate where, depending on the phase diagram for the boron-molybdenum system, precipitation of B-Mo intermetallic phases may occur.

2.1 Recrystallization

For the underlying TZM, melting is unlikely given the 2620^{o}C required for this to occur; however, recrystallization may occur at a far lower temperature [9]. For a deformed (cold worked) metal, such as TZM after being thermomechanically processed and/or machined, the energy of the cold work is stored in residual stresses and the dislocation structure induced by the cold work. When heated, the TZM will release some of this stored energy through recrystallization. This process begins with the nucleation of new grains at areas of high local stresses near the grain boundaries. The

majority of the time required for recrystallization is spent in the nucleation phase. Following nucleation, the newly formed recrystallized grains will grow, reducing the stresses at their boundaries and releasing further stored energy[21].

The amount of excess energy available will depend on the amount of cold work in the material. The higher the amount of cold work, the lower the temperature at which recrystallization will occur, to a point. Beyond approximately 70% cold work, the recrystallization temperature ceases to drop, resulting in a minimum recrystallization temperature. For this reason, there will be a range of recrystallization temperatures that is dependent upon cold work. The upper temperature is limited by an insufficient amount of cold work energy available to surmount the activation energy barrier for nucleation of new grains. Figure 2-1 shows the recrystallization temperature of TZM (Mo-0.49Ti-0.057Zr) as the uppermost curve . Figure 2-1 also illustrates another key factor in the overall recrystallization behavior of a material. Since the process consists of nucleation and growth, an activation energy will be required. As a result, there will be a time at temperature dependence of the process. The recrystallization temperature data shown in Figure 2-1 is thus reported for a one hour isothermal anneal and represents the onset of recrystallization [14].

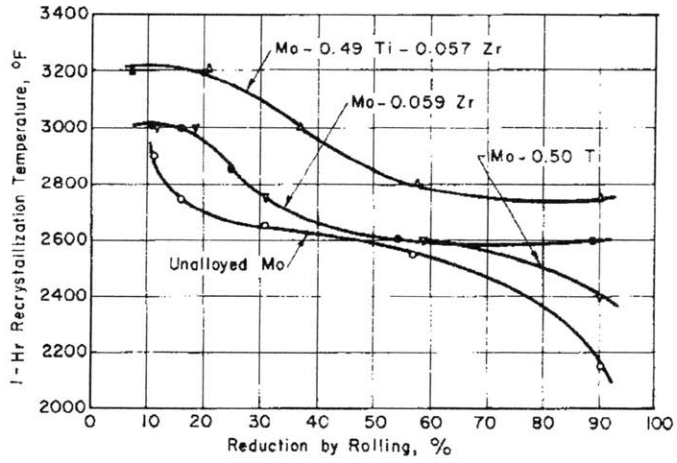

Figure 2-1: Recrystallization temperature as a function of cold work, represented by percent reduction in bar thickness during rolling, for several molybdenum alloys. These data represent the onset of recrystallization, following nucleation, for a one hour isothermal anneal. The behavior of TZM is given by the uppermost curve.

[14]

The time dependence of the recrystallization process is further illustrated in Figure 2-2, which shows the degree (%) of recrystallization as a function of temperature for a fixed time at that temperature [15]. Once nucleation has occurred, the recrystallized grains will grow and consume the original material, with 100% recrystallization achieved when all of the original material is consumed. At this point, if there is sufficient energy available (supplied by the temperature), the new grains will grow by consuming each other until an equilibrium final grain size is achieved [21].

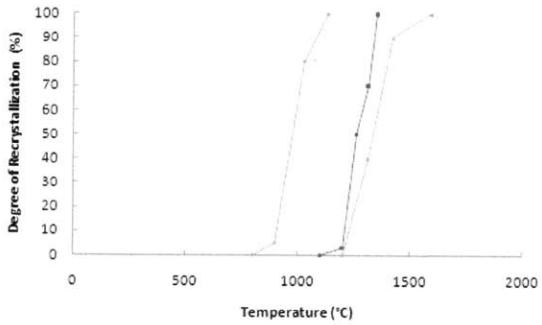

Figure 2-2: The degree of recrystallization versus temperature for a one hour duration of heating for molybdenum (blue), TZM (red), and tungsten (green). Note that the degree of recrystallization for all three alloys increases dramatically over a relatively small range of temperatures.
[15]

A further illustration of the time dependence of the process is illustrated in Figure 2-3, which shows the effect of time at temperature on the onset of recrystallization (the end of the nucleation process) in TZM [15]. Figures 2-1 and 2-2 are for isothermal annealing times of one hour; however, the temperature quoted represents the mean of a Boltzmann energy distribution where the energy at the tail of the distribution is considerably higher. This, when combined with the statistical nature of the distribution, results in a time at temperature dependence of the recrystallization temperature [21].

As shown in Figure 2-3, the recrystallization temperature increases as the duration of heating decreases. The range of recrystallization temperatures also decreases with decreasing time of heating. This is important to note, as the degree of recrystallization increases dramatically over a relatively narrow range of temperatures, as shown in

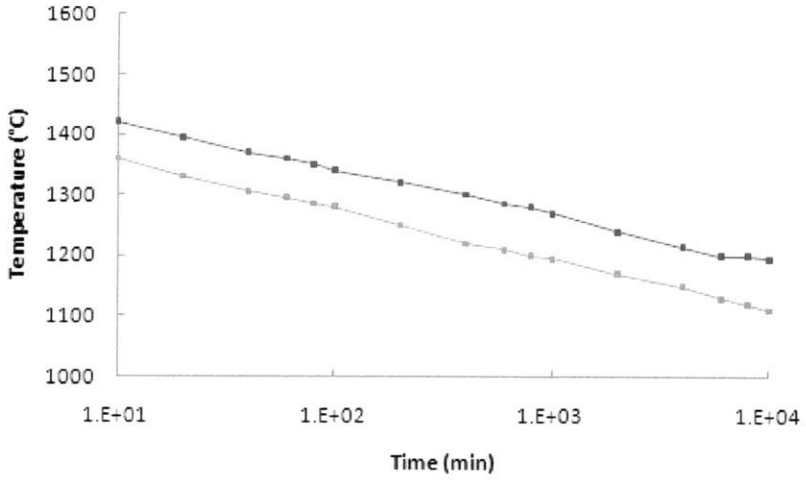

Figure 2-3: Recrystallization temperature of TZM as a function of the duration of isothermal heating, with the temperature representing the onset of recrystallization, following nucleation. The red curve is the upper temperature bound and the blue curve is the lower temperature bound for the range of recrystallization temperatures. [15]

Figure 2-2 [15]. Given the lack of such data for the timescales of interest in this study (~1ms), the data in Figure 2-3 have been extrapolated back to these timescales by plotting the upper and lower bounds of the recrystallization temperature range against the logarithm, in base 10, of the time at temperature. The equations fitted to the upper and lower bounds of the recrystallization temperature range for TZM are

$$T_{upper} = -75.39 * \log(t) + 1593.23 \tag{2.1}$$

and

$$T_{lower} = -78.31 * \log(t) + 1571.48, \tag{2.2}$$

where T_{upper} is the upper temperature bound and T_{lower} is the lower temperature bound, in ^{o}C, for a given time t, in seconds. Applying Equations 2.2 and 2.1, the range of recrystallization temperature for an isothermal heating event of 1ms is 1806-1819^{o}C. This temperature range should be compared with the recrystallization temperature data presented in Figure 2-1. While the data in Figure 2-1 are for a one

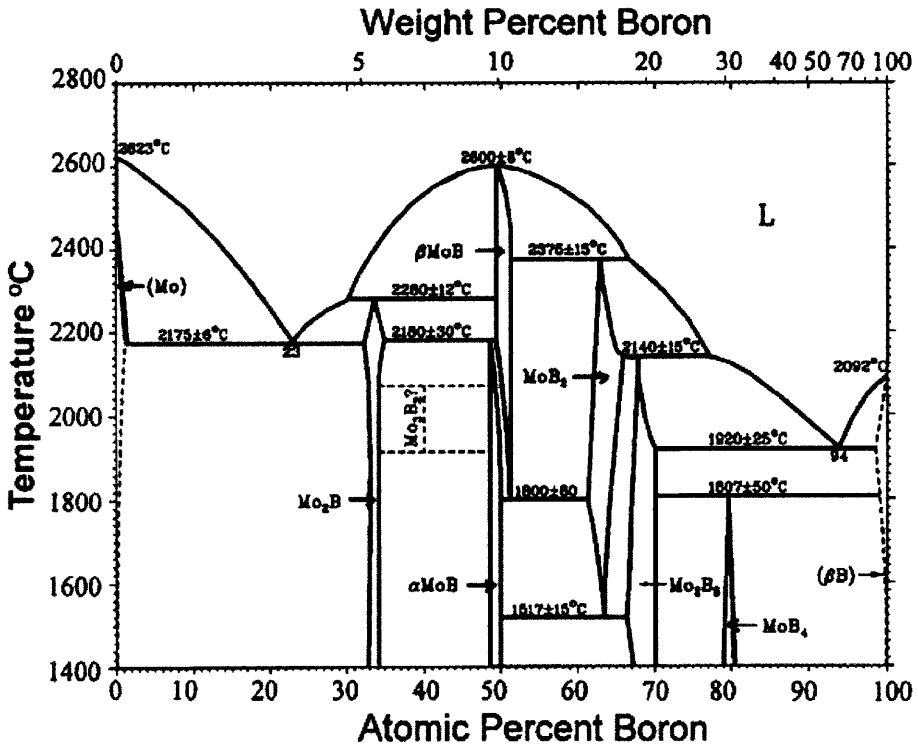

Figure 2-4: Boron-molybdenum phase diagram, indicating the compositions and temperatures at which several common intermediate B-Mo phases are stable. Such phases may be formed as precipitates by boron diffusion into the underlying molybdenum of the tiles at high temperature.
[16]

hour anneal, the extrapolated temperature is at least approximately comparable.

2.2 Intermetallic Phase Precipitation

Higher temperatures at the tile surface may also cause the boron to diffuse into the TZM substrate, where it can combine with the molybdenum matrix to form various B-Mo phases. The B-Mo phase diagram shown in Figure 2-4 shows several of these intermediate B-Mo phases, as well as the compositions and temperatures at which they are stable [16].

In order to discover evidence of these processes, a number of analytical materials science techniques must be employed. Measurement of the boron distribution at the tile surface is best done using ion beam analysis (IBA) techniques, such as par-

ticle induced gamma emission (PIGE) and Rutherford back scattering (RBS). The microstructure of the TZM substrate, on the other hand, is best studied through optical and scanning electron microscopy (SEM), along with energy dispersive X-ray spectroscopy (EDX). Additionally, X-ray diffraction (XRD) is necessary to detect the presence of the B-Mo phases shown in Figure 2-4. These techniques are explained in detail in following sections.

2.3 Estimated Transient Temperature

The data gathered from the above analysis and measurements may be used to estimate the nature of the plasma-tile interaction, as well as to predict the behavior of other tile-film systems in a similar environment. For example, if recrystallization is observed on the exposed tile surface, then the range of exposure temperatures can at least be bracketed, keeping in mind the uncertainties associated with the data available and the short exposure time for the actual case relative to the available data. If intermetallic phases are detected that were not present in the unexposed condition then, given the specific characteristics of these phases, especially temperature and composition ranges of stability, the exposure temperature during the plasma transients can be further bracketed.

2.4 Ion Beam Analysis (IBA)

Ion beam analysis is a relatively broad field of materials research which encompasses a number of analytical techniques. As the name implies, the unifying element in these techniques is the use of a beam of ions, typically accelerated to energies on the order of MeV, to irradiate a specimen. The interactions between these ions and the atoms composing the specimen produce a variety of forms of secondary radiation, which may be measured spectroscopically and used to deduce the properties of the specimen. While there are many IBA methods, the two of interest in this thesis are particle induced gamma emission and Rutherford back scattering.

2.4.1 Particle Induced Gamma Emission (PIGE)

Particle induced gamma emission makes use of the nuclear reactions that occur when charged particles, such as protons, interact with nuclei within a sample, resulting in the emission of gamma radiation. The spectrum developed by detection of these gamma rays provides much insight into the composition of the sample. The energies of the emitted gamma rays are dependent upon the elements present, and the relative intensities of these different gamma rays provide information on the elemental percent composition. The depth of analysis available with PIGE is somewhat limited, as a beam of light ions, such as protons, with energy on the order of a few MeV will typically not be able to penetrate greater than 50 μm below the surface of a specimen. PIGE is also best used for samples primarily composed of lower Z elements since the Coulomb barrier between the beam particles and sample nuclei increases with Z [17]. Therefore, PIGE is best suited for analysis of thin films composed of low Z materials, as is the case with the boron film on the Alcator tiles.

In addition to bulk composition, PIGE may be used to perform depth profiling for certain elements, particularly those lower in Z, up to the limit of the beam's penetration depth. This is possible because most of the lighter nuclei, or those with Z<30, have sharp, pronounced resonances for gamma emitting nuclear reactions induced by light ions with energies less than ~3MeV [17]. For ^{10}B, the boron isotope responsible for the 432keV gamma ray used to measure boron concentration, such a sharp resonance occurs at a proton beam energy of approximately 1.5MeV, as shown in Figure 2-5 [18]. If the energy of the proton beam at the surface of a specimen containing boron is varied, it will cause the 1.5MeV resonance energy to be reached at different depths within the tile. The intensity of the 432keV gamma emission may then be plotted versus the depth at which the protons reach the resonant energy, creating a curve which is directly proportional to the areal density of boron nuclei at the various depths.

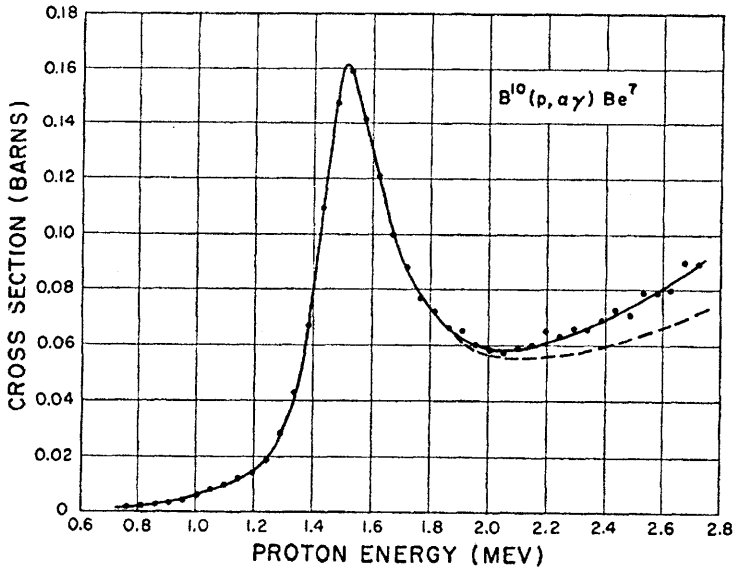

Figure 2-5: Cross section for proton-induced emission of the 432keV gamma ray by ^{10}B. Note the sharply peaked resonance that occurs at 1.5MeV.
[18]

2.4.2 Rutherford Back Scattering (RBS)

Rutherford back scattering is another IBA technique that may be used to explore the composition and depth profile of a specimen. RBS occurs when an energetic particle from the ion beam elastically collides with a nucleus within the target, scattering back from the target and transferring a portion of its energy to this nucleus. According to classical conservation laws, the fraction of the initial energy lost by the incident ion during RBS is given by

$$k = \left(\frac{m\cos(\theta) + \sqrt{M^2 - m^2(\sin(\theta))^2}}{m + M} \right)^2, \tag{2.3}$$

where k is the fraction of the incident particle's initial energy that is transferred, m is the mass of the incident particle, M is the mass of the target nucleus receiving energy from the incident particle, and ϑ is the scattering angle in the laboratory frame of reference. It must be noted that Equation 2.3 only applies for an incident particle that is less massive than the target atom, or m<M; otherwise, backscattering will not occur. By using an ion beam with particles of known mass and energy, then detecting

the backscattered particles and measuring their energy, Equation 2.3 can be used to determine the mass of the scattering atom [19].

RBS may also be used to create a compositional depth profile for a sample. As described above, a backscattered particle should have a specific energy determined by the target atom's mass and the scattering angle. In reality, the incident particles interact continuously with the electrons throughout the sample, losing energy to these electrons both before and after the backscattering collision [19]. This continuous energy loss over distance as a particle travels through a medium is referred to as the stopping power of the medium. This stopping power may be calculated as

$$-\frac{dE}{dx} = \frac{4\pi e^4 z^2}{m_0 v^2} NZ \left[\ln \frac{2m_0 v^2}{I} - \ln\left(1 - \frac{v^2}{c^2}\right) - \frac{v^2}{c^2} \right], \tag{2.4}$$

where -dE/dx is the stopping power, e is the fundamental electron charge, z is the atomic number of the incident particle, m_0 is the rest mass of an electron, v is the velocity of the incident particle, N is the number density of atoms in the target, Z is the atomic number of the atoms in the target, I is the average excitation and ionization potential of atoms in the target, and c is the speed of light [20]. Using this relation, the additional energy loss beyond that of the backscattering collision may be used to divide the sample into layers of various composition.

Despite the capabilities of RBS, there are limitations to the measurements that may be attempted. Differentiating Equation 2.3 with respect to M results in

$$\frac{dk}{dM} = \frac{2M\left(m\cos(\theta) + \sqrt{M^2 - m^2(\sin(\theta))^2}\right)^2}{(m+M)^4\sqrt{M^2 - m^2(\sin(\theta))^2}}, \tag{2.5}$$

where dk/dM is the rate of change in energy transferred by the incident particle with respect to the target atom's mass. According to Equation 2.5, the differences in the energy of particles backscattered by different atoms become less pronounced as the target atoms become heavier. Once these differences become less than the resolution of the detectors used for measuring backscattered particle energy, it is impossible to discern between heavier elements. Unfortunately, this resolution issue at higher atomic masses, which generally accompany higher Z, is juxtaposed with a

low probability of RBS occurring for lower Z targets. This is due to the behavior of the RBS cross-section,

$$\sigma = \left(\frac{zZe^2}{4E}\right)^2 \frac{4}{(\sin(\theta))^4} \frac{[\sqrt{1-((m/M)\sin(\theta))^2}+\cos(\theta)]^2}{\sqrt{1-((m/M)\sin(\theta))^2}}, \tag{2.6}$$

where σ is the cross-section for RBS, E is the initial energy of the incident particle, and all other symbols are the same as for Equation 2.4. As shown in Equation 2.6, the probability of RBS increases as the square of Z for the target atom, and so it is difficult to obtain appreciable detection rates for backscattered particles that interact with low Z elements. Thus, RBS is optimal for materials with Z in the range of 10 to 18; however, if only one high Z element is present, it will be readily detected and sufficiently distinct from any low Z constituents [19].

2.5 Scanning Electron Microscopy (SEM)

SEM greatly extends the magnification and depth of field available for microstructural analysis beyond that of an optical microscope. While optical microscopes are limited to approximately 1500X magnification, the typical SEM can achieve magnification in excess of 50,000X. Also, the depth of field of an SEM may be as great as 300 times that of an optical microscope, allowing for better viewing of particularly deep features, as encountered in heavily etched specimens and fracture surfaces. Although optical microscopes offer superior resolution at magnifications below 300-400X for specimens that are relatively flat, the SEM is preferred at higher magnifications and for specimens with greater surface relief [21].

SEM micrographs are formed by scanning an area of the specimen, known as the raster, with a pointed beam of electrons in a series of line scans. The electrons in this beam interact with the raster to produce a number of emissions, such as backscattered beam electrons, secondary electrons from the specimen, and X-rays. Almost any of these emissions may be used to infer the texture of the raster; however, the secondary electrons are typically used because they generally originate at the narrow point of the beam, and so they offer the highest resolution. To generate an image of

the specimen, a detector is used to measure the intensity of secondary electrons produced at each location in the scan. This intensity determines the brightness of the corresponding location on the cathode ray tube. Since attenuation of secondary electrons is a function of distance, the contrasting levels of brightness can provide an indication of specimen topography. Unfortunately, contrast also occurs for different materials adjacent to one another, and so discriminating between geometrical and compositional features can be difficult [21].

2.6 Energy Dispersive X-Ray Spectroscopy (EDX)

Like PIGE and RBS, EDX is a common method for evaluating the elemental composition of a specimen. In EDX, a beam of high energy charged particles or X-rays is focused into the specimen. In many cases, EDX instruments are coupled with an SEM, and so the two devices share the same electron beam. As the beam impinges upon the specimen, it will eject electrons from the inner shells of atoms in the specimen, creating a vacancy which will be filled by an outer orbital electron. When this electron transitions to an inner orbital, it will emit a characteristic X-ray that is equal in energy to the difference between the inner and outer shells. The energy of a characteristic X-ray is particular to a specific shell transition in an atom of a given element. Thus, by using an X-ray detector to collect an energy spectrum, the elemental composition of a specimen may be determined through the energies of the characteristic X-rays observed. Unfortunately, the characteristic X-rays emitted by lower Z elements are so low in energy as to be absorbed by the detector window, and so elements lower in Z than carbon cannot typically be detected with EDX [21].

2.7 X-Ray Diffraction (XRD)

X-ray diffraction is yet another technique available for compositional analysis; however, it goes beyond the elemental analysis of the previously described techniques by allowing for identification of the crystalline structures present in the specimen. This

allows for the detection of particular compounds and phases that are present in the sample. XRD is best understood by considering the wavelike behavior of X-rays and other electromagnetic radiation. According to classical physics, any wave encountering an array of regularly spaced scatterers will undergo Bragg diffraction. This occurs because the interaction between the wave and each scatterer creates isotropic secondary waves, originating at the scatterers. For the most part, these waves are out of phase and undergo destructive interference; however, some waves will be in phase in a few directions and interfere constructively. This results in an increase in wave amplitude in these directions, with destructive interference correspondingly reducing the amplitude in all others. The directions of constructive interference are a function of the wavelength and the interval between scatterers.

In the case of X-ray diffraction, the scatterers are the electrons surrounding the constituent atoms in the sample. For any crystalline solid, these atoms are found at particular locations in the lattice, forming a series of scattering planes with a constant distance of separation. Thus, a beam of X-rays will diffract in such a sample, producing a reflected wave of maximum intensity when the beam is incident upon the sample at particular angles. The angles necessary to produce this maximum reflected wave are given by Bragg's law,

$$n\lambda = 2d\sin\theta, \tag{2.7}$$

where n is any whole number, λ is the wavelength of the incident X-rays, d is the spacing between scattering planes, and θ is the angle of incidence necessary to maximize the intensity of the reflected wave, also known as the Bragg angle. It should be noted that appreciable diffraction is only observed when λ and d from Equation 2.7 are similar. Due to this constraint, X-rays (λ=0.1-100Å) are the only form of electromagnetic radiation suitable for diffraction crystallography, but electron and neutron diffraction are also sometimes used [22].

In practice, XRD is performed with the X-ray beam in a fixed position. The specimen is then rotated through a range of angles relative to the incident beam, and

the intensity of the reflected wave is measured at each angle. This reflected wave is often measured as twice the incidence angle, or 2ϑ, relative to the X-ray beam. This produces a spectrum of reflected wave intensity versus twice the Bragg angle, with the locations of local maxima being used in Equation 2.7 to determine spacings between planes in the lattice. Such spectra have already been recorded and catalogued for myriad compounds and isomers, and so phase identification is largely a matter of fitting the measured spectrum from a particular sample with those in the XRD databases; however, the prodigious amount of differing compounds and phases with relatively few allowable crystal structures requires some discrimination based upon the results of the elemental composition methods described above [22].

2.8 Determination of Plasma Properties

The data gathered from the previously described techniques may be used to determine the properties of the plasma itself. Specifically, they allow an approximation of the temperature gradient at the tile surface to be made. This temperature gradient may be used to determine the local heat flux through the heat diffusion equation,

$$\rho c_p \frac{dT}{dt} = \nabla \cdot (k \nabla T), \tag{2.8}$$

where ρ is the material density, c_p is the specific heat capacity of the material, dT/dt is the time derivative of the temperature, k is the coefficient of thermal conductivity for the material, and ∇T is the temperature gradient in the medium [23]. Assuming a semi-infinite solid with a constant heat flux, this equation may be solved in one dimension to obtain

$$T(x,t) = \frac{2q}{k} \left\{ \left(\sqrt{\frac{kt}{\pi \rho c_p}} \right) e^{-x^2 \rho c_p / 4kt} - \frac{x}{2} erfc \frac{x}{2} \sqrt{\frac{\rho c_p}{kt}} \right\}, \tag{2.9}$$

where q is the local heat flux, x is the depth below the heated surface, and erfc is the complementary error function [24]. Equation 2.9 may be simplified by defining a new variable

$$u \equiv \frac{x}{2}\sqrt{\frac{\rho c_p}{kt}} \tag{2.10}$$

such that the heat diffusion solution may be written as

$$T(x,t) = 2q\sqrt{\frac{t}{\pi \rho c_p k}}\left(e^{-u^2} - 2u\int_u^\infty e^{-\xi^2} d\xi\right), \tag{2.11}$$

where ξ is a placeholder variable in the integral term which represents the complementary error function [25]. The form of this equation is a rapidly decaying exponential in which the majority of the thermal loading occurs within a relatively thin layer below the surface. The thickness of this layer, known as the skin depth, may be approximated by

$$\delta = \sqrt{\frac{kt}{\rho c_p}}. \tag{2.12}$$

Once the heat flux is known, it may be used to calculate the product of the temperature and particle flux of the plasma according to the equation

$$q_{parallel} = \gamma \Gamma k_B T_e, \tag{2.13}$$

where $q_{parallel}$ is the heat flux parallel to the magnetic field lines, γ is the total sheath heat transmission coefficient, Γ is the particle flux, $k_B$is the Boltzmann constant, and $T_e$is the temperature of the plasma sheath. This parallel heat flux may then be converted to the local heat flux incident on the tiles by the relationship

$$q = q_{parallel}\sin(\theta), \tag{2.14}$$

where θ is the angle of incidence between the tile surface and the magnetic field lines. The value of the total sheath heat transmission coefficient is approximately 7, $k_B$is equal to 8.617×10^{-5}eV/K, $T_e$is typically within the range 1-3x10^5K, and θ is between 1^o and 10^o for undistorted tiles. Γ depends upon the temperature and number density of the plasma according to the equation

$$\Gamma = n_e \sqrt{\frac{k_B T_e}{m_i}}, \tag{2.15}$$

where $n_e$is the plasma number density, typically $<10^{20}$particles/m^3, and m_i is the mass of the deuterons, 1875.6MeV/c^2 [6]. Once the local heat flux has been determined from the data and Equation 2.11, the relationship between temperature and number density of the plasma may be approximated using Equations 2.13, 2.15, and 2.14.

Chapter 3

Materials and Methods

A fairly diverse set of data is necessary to fully determine the nature of the damage present in the boronized TZM tiles from Alcator C-Mod. A number of tiles with varying degrees of apparent damage were removed from the limiter and divertor and photographed for macroscopic characterization. Modeling was also performed using the expected heat and particle fluxes at the tile surface, along with the thermal transient history of the tiles, to estimate the depth of damage from each of these sources. These results were compared to data gathered during analysis of the tiles through several techniques, including PIGE, RBS, optical microscopy, SEM, EDX, and XRD. A detailed description of the modeling and analysis of these tiles may be found in the following sections.

3.1 Tile Selection and Macroscopic Characterization

A number of tiles with different macroscopic manifestations of damage were selected for analysis, as well as one tile, 070B40809R, with no apparent damage. These tiles, and their locations in Alcator C-Mod, are provided in Table 3.1. The poloidal locations of the damaged tiles are also indicated in Figure 3-1. 070B40809R, however, was installed in an earlier configuration of Alcator and removed in June 2004, so its

Tile	Location
A41171I	Row 7 of Divertor, Between C and D Port
A41258I	Row 7 of Divertor, Between C and D Port
G7	GH Limiter, Left Edge
G20	GH Limiter, Right Edge
G13S	GH Limiter, Left Edge
G15S	GH Limiter, Left Edge
070B40809R	Ceiling Module, Outer Edge Between K and A Port

Table 3.1: List of tiles removed from Alcator C-Mod for analysis, along with their locations within the reactor during the 2008 campaign.

location is shown in Figure 3-2. The four tiles from the GH limiter are all recessed in major radius due to their locations at the limiter edges. These locations are shown on the GH limiter map in Figure 3-3, and the recessed edges may be seen in the photograph of the GH limiter, provided in Figure 3-4.

The recessed edges of of the GH limiter are also illustrated by the radial profile of the edge tiles, such as G15S, shown in Figure 3-5. As shown in this view, the bottom of the tile is mounted to the limiter module with the opposite side facing the plasma. The rounded side of this plasma facing surface is located at the edge of the limiter module, with the flat side nearer to the center of the module. This flat side is parallel to the magnetic field lines, and so the tile surface is recessed away from the plasma at the rounded portion that is at the edge of the module. Photographs of the damaged surfaces are shown in Figure 3-6. It is interesting to note that the melting which appears to have occurred at the surfaces of several tiles produced a rough texture, rather than a smooth melt layer. This is believed to be a result of the surface tension of melted boron and molybdenum.

3.2 Modeling

Thermal and radiation modeling was done to determine the depth of interaction in the tiles for each form of damage. The depth of thermal damage was estimated from the skin depth calculated with Equation 2.12. Radiation damage was approximated using the Stopping of Radiation in Matter (SRIM) software. For both forms of damage,

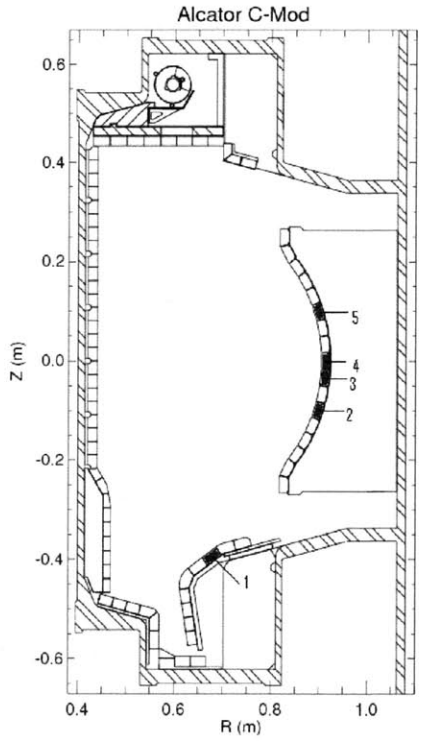

Figure 3-1: The poloidal locations of the damaged Alcator tiles (1) A41171I and A41258I, (2) G20, (3) G15S, (4) G13S, and (5) G7.

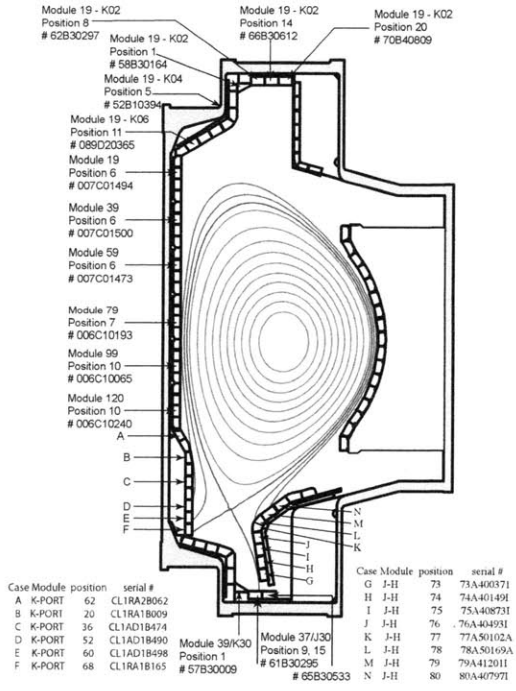

Figure 3-2: The poloidal location of the undamaged tile 070B40809R, indicated in the top right corner of the schematic.

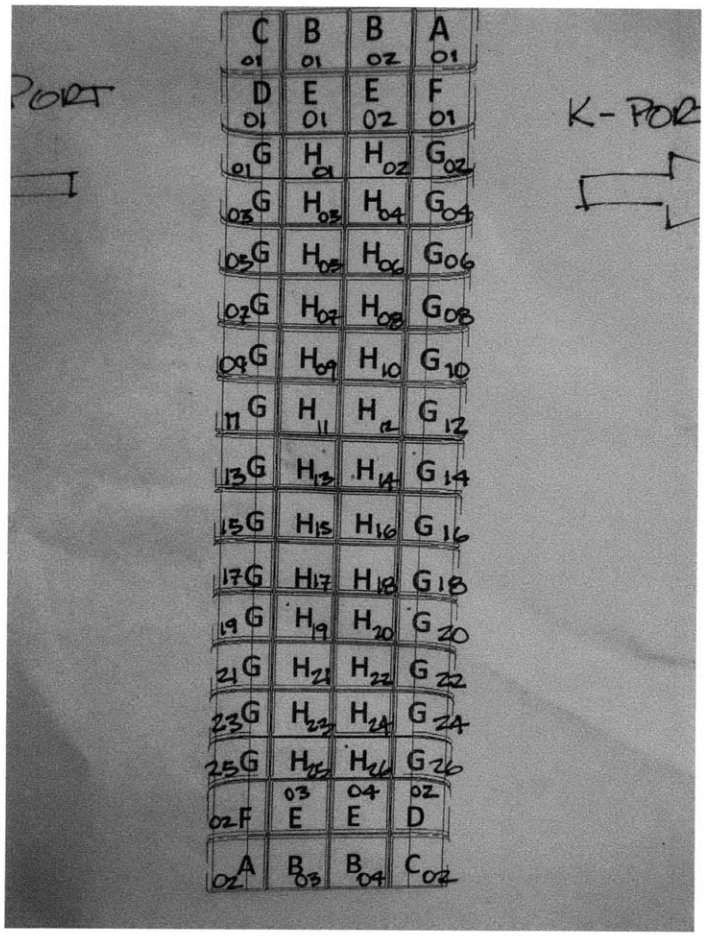

Figure 3-3: A map of the GH limiter, showing the locations of tiles G7, G13S, G15S, and G20.

Figure 3-4: A photo of the GH limiter, showing the tiles along the left and right edges recessed in major radius.

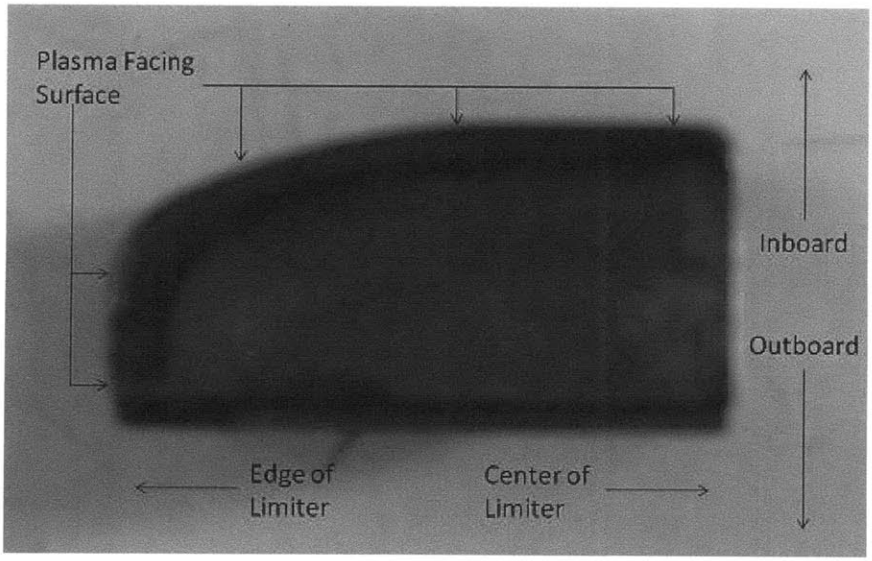

Figure 3-5: A radial view of G15S, a tile from the left edge of the GH limiter module. The magnetic field lines are parallel to the flat plasma facing surface on the side of the tile nearer the center of the limiter, with the rounded side nearer the edge of the limiter receding away from the plasma.

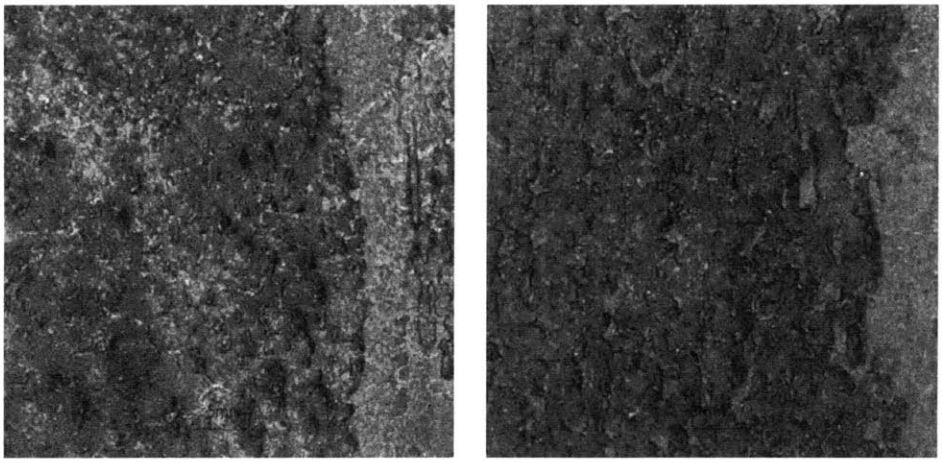

(a) A41171I

(b) A41258I

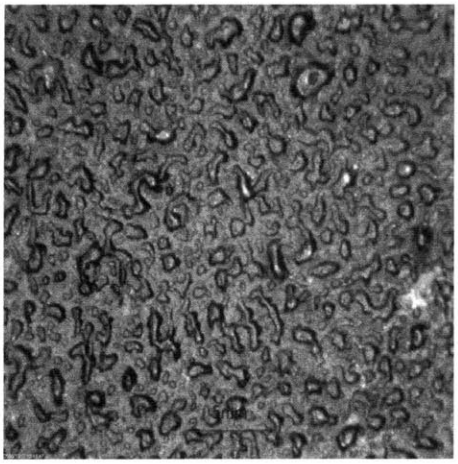

(c) G7

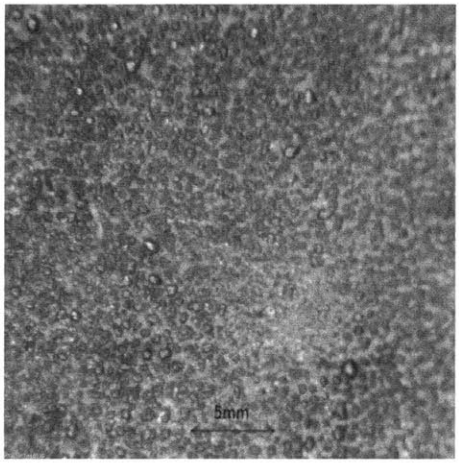

(d) G20

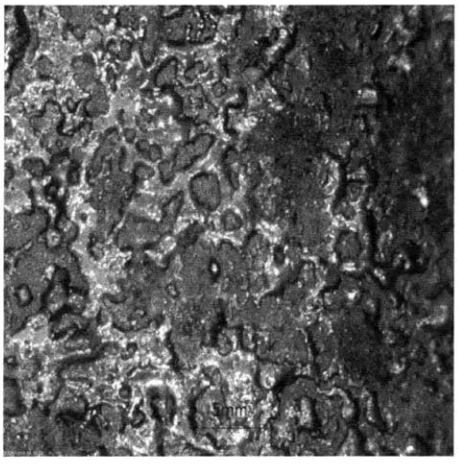

(e) G13S

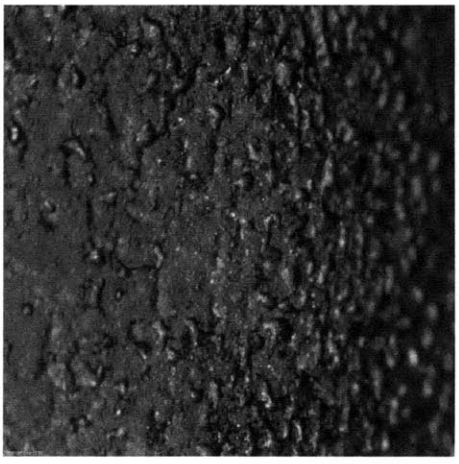

(f) G15S

Figure 3-6: Macrophotographs of the damaged surfaces of tiles used in this investigation.

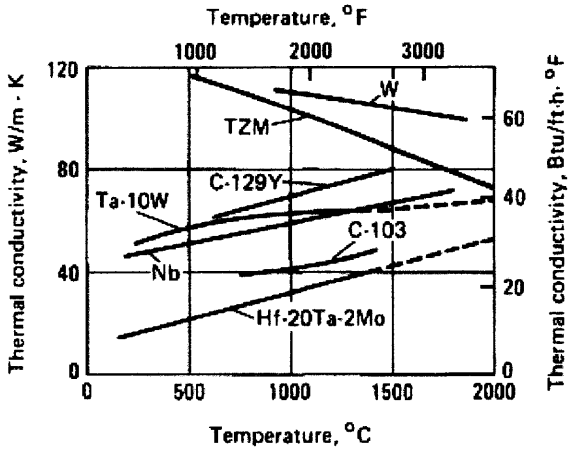

Figure 3-7: Thermal conductivity of TZM versus temperature. [9]

calculations were performed based upon normal plasma parameters during a pulse of ~1s as well as disruptions on the millisecond timescale.

3.2.1 Thermal Damage

The depth of thermal damage may be modeled using the skin depth, calculated with Equation 2.12. The values of k, ρ, and c_p used in this equation are based upon a range of effective concentrations of boron and molybdenum. The room temperature density and specific heat capacity of pure boron are 2.31g/cm^3 and 1.026J/g·K, respectively. For TZM, the room temperature values for density and specific heat capacity are 10.16g/cm^3 and 0.251J/g·K, respectively [9]. A typical value of the thermal conductivity of pure boron is 27.4W/m·K. In the case of TZM, the thermal conductivity decreases markedly with increasing temperature, as shown in Figure 3-7 [9].

For these models, the k for TZM is assumed to be a constant 100 W/m·K based upon Figure 3-7 [9]. It is also possible that various molybdenum borides, such as those shown in Figure 2-4, have been formed at the boron-TZM interface, each with its own thermal conductivity coefficient. Nonetheless, the values for these coefficients appear to be similar to those for boron or also TZM at higher temperatures, with the thermal conductivity of Mo_2B_5 ranging from 50.3 to 27.2W/m·K at temperatures of 20 and 900^{o}C, respectively [26]. Given this similarity in thermal conductivity, as well

Effective B Concentration	ρ_{eff} (g/cm^3)	$c_{p,\,eff}$ ($J/g \cdot K$)	k_{eff} ($W/m \cdot K$)	Depth of Heat Penetration (mm) Full Pulse Timescale (1s)	Depth of Heat Penetration (μm) Transient Timescale (1ms)
0	10.16	0.251	100	6.26	198
0.2	8.59	0.406	85.48	4.95	157
0.4	7.02	0.561	70.96	4.25	134
0.6	5.45	0.716	56.44	3.80	120
0.8	3.88	0.871	41.92	3.52	111
1	2.31	1.026	27.4	3.40	108

Table 3.2: Estimated depths of thermal damage for both full pulse and transient timescales in tiles with given near surface concentrations of boron.

as the difficulty in predicting the concentration of these intermediate phases at the tile surface, their contributions are not considered in this model.

The depth of thermal damage for timescales of both a full plasma pulse (1s) and a transient disruption (1ms) are presented in Table 3.2. These depths are estimated for a number of compositions of boron and TZM, with weighted effective values of ρ, c_p, and k given for each. From Table 3.2, it may be seen that reducing the timescale from seconds to milliseconds reduces the skin depth for heat diffusion from several millimeters to just 100-200μm.

3.2.2 Radiation Damage

The depth of radiation damage was estimated using SRIM, a software program which models the interactions of radiation in matter [27]. The particle fluxes in Alcator are generally $\sim 10^{22}$ particles/m^3, with energies in the range of 10-100eV. Assuming a maximum particle energy of 100eV and a boron film thickness of 5μm, the estimated depth of radiation damage using SRIM is ~30nm, confining this damage to the boron film. These particles also cause substantial damage to the boron film through sputtering, with approximately one sputtered boron atom for every thirteen deuterons at 100eV. During the course of a campaign, this sputtering is sufficient to erode 1-2μm of the boron film from the tile surfaces.

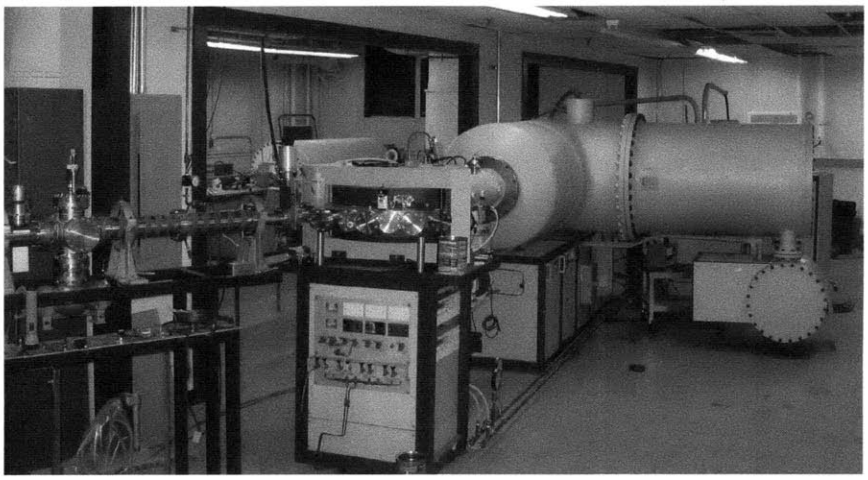

Figure 3-8: The 1.7MV Tandetron accelerator at the CLASS facility. [7]

3.3 Ion Beam Analysis

All ion beam analysis measurements were conducted at the Cambridge Laboratory for Accelerator Study of Surfaces (CLASS) using a 1.7MV Tandetron tandem accelerator, shown in Figure 3-8 [7]. Tandem accelerators are essentially two linear accelerators in series which share the same power supply. In such accelerators, negative ions are produced by a source at one end and accelerate toward the high voltage terminal, located halfway down the accelerator. At this terminal, the electrons are stripped from the ions, and the newly positive ions accelerate away from the high voltage terminal. Following this acceleration, the ions are focused into a narrow beam by a quadrupole magnet, and then channeled into the appropriate beamline by a high energy steering magnet.

For the Tandetron at CLASS, the negative ions are produced using a cesium sputtering source and a variety of targets, such as titanium hydride (TiH_2) for negative hydrogen ions, and then separated from other ions and directed into the accelerator by a low energy steering magnet. The electrons are stripped from these ions as they pass through nitrogen gas that is injected at the high voltage terminal. The major components of the Tandetron are indicated in the accelerator schematic in Figure 3-9 [7]. All of the IBA techniques performed for the Alcator tiles were done with proton beams at 2MeV. For singly charged ions such as protons, the accelerator's voltage

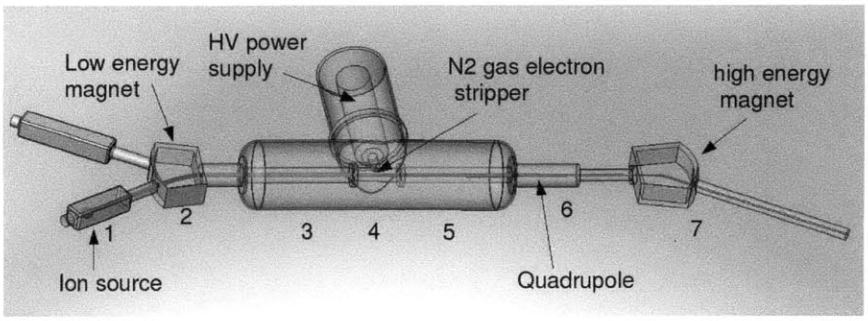

Figure 3-9: Schematic of the Tandetron accelerator, indicating the locations of the (1) ion source, (2) low energy steering magnet for ion selection, (3) path of negative ion acceleration, (4) high voltage terminal with electron stripping occurring in nitrogen gas, (5) path of positive ion acceleration, (6) quadrupole focusing magnet, and (7) high energy steering magnet.
[7]

limit of 1.7MV represents a maximum allowable beam energy of 3.4MeV.

3.3.1 Particle Induced Gamma Emission

PIGE measurements were made at several damaged surface locations on all of the tiles listed in Table 3.1. The surface regions of the tiles are referenced to the tile photographs shown in Figure 3-10. Unfortunately, no photograph is available for the regions of G20 used in these measurements since this tile had already been sectioned and some pieces prepared for microscopy. For each measurement, the region of the tile under investigation was irradiated with a beam of 2MeV protons and the induced gamma radiation collected with a NaI detector over a detector live time of approximately 100s. These examinations were all performed externally; that is, the targets were placed before the beam on a shelf open to the atmosphere, separated from the beam line at vacuum by a Kapton window 7.5μm thick. The number of counts in the 432keV ^{10}B photopeak were recorded for each region, as well as the total charge of the incident protons. A baseline measurement was also made using a block of boron nitride (BN) as a target.

In order to determine the concentration of boron in each region, a code was written to simulate the rate of 432keV gamma emission for a 2MeV beam of protons incident upon targets with varying concentrations of boron and molybdenum. This same code

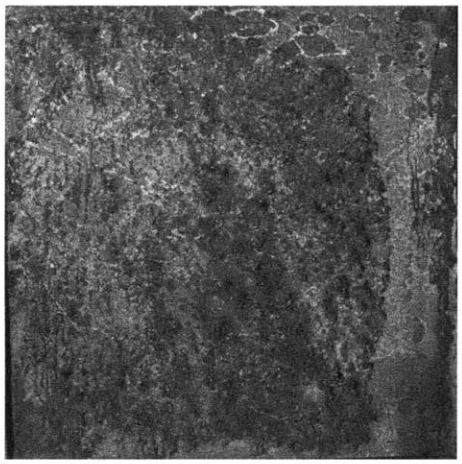

(a) A41171I

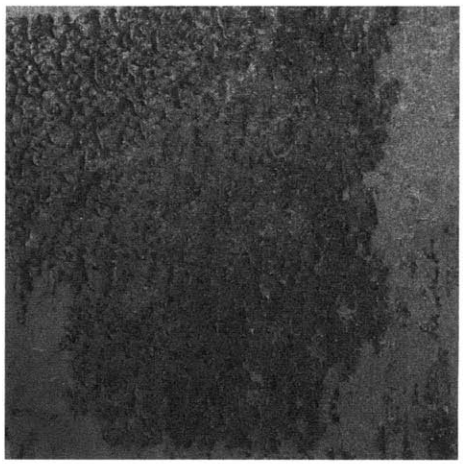

(b) A41258I

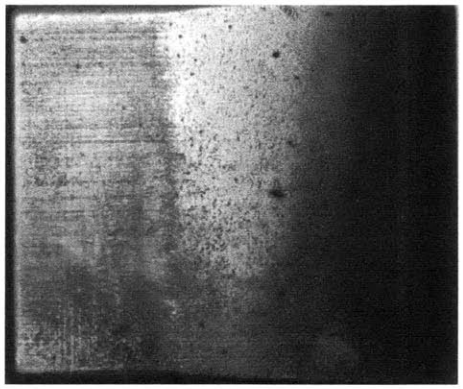

(c) G7

(d) G13S

(e) G15S

Figure 3-10: Photographs of the entire tile surface for tiles used in IBA. All tile surface locations are referenced to these photographs. For the limiter tiles G7, G13S, and G15S, the right hand side in these photographs is the rounded edge of the tile which would be at the edge of the GH limiter, as shown in the radial view of G15S provided in Figure 3-11. Note that the limiter tiles in these photographs are in opposite orientation to their installed location, as shown in Figure 3-11.

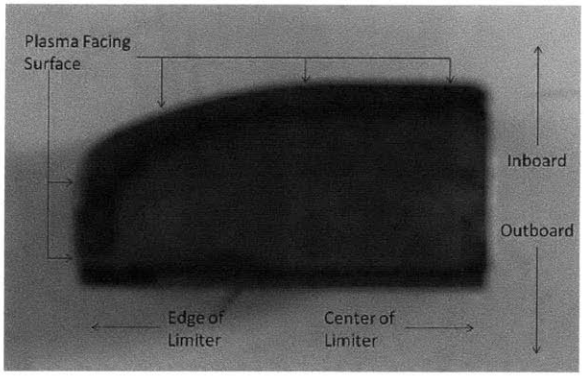

Figure 3-11: A radial view of G15S, a tile from the left edge of the GH limiter module. The magnetic field lines are parallel to the flat plasma facing surface on side of the tile nearer to the center of the limiter, with the rounded side at the edge of the limiter receding away from the plasma. Note that the orientation of the tile in this view is equivalent to that when installed in the limiter module, but opposite the orientation of the limiter tile photographs shown in Figure 3-10.

was used to determine the counting rate for 432keV gammas when a 2MeV beam was used to irradiate a target of boron nitride. The energy of the proton beam was modeled by interpolating the stopping powers of the various target materials, as well as the 7.5μm Kapton window, using tables generated by SRIM. Interpolation was also necessary for the 432keV emission cross-section, as shown in Figure 2-5 [18]. The modeled counting rates for the various B-Mo targets were normalized to the modeled rate for BN.

Similarly, the observed counts from the PIGE measurements of each region were normalized to the corresponding counts recorded with the BN block as a target. Unlike in the simulation, the beam current in the PIGE measurements was not consistent, and so the recorded counts were normalized by incident charge as well as the counts recorded from BN. These fully normalized recorded counts were interpolated among the normalized count rates from the simulation, resulting in a boron concentration for each region, down to a penetration depth of ~30μm as predicted by SRIM.

3.3.2 Rutherford Back Scattering

RBS measurements were made for all of the tiles except G20 because the sections of this tile could not be properly mounted in the specimen holder. Unlike PIGE, these

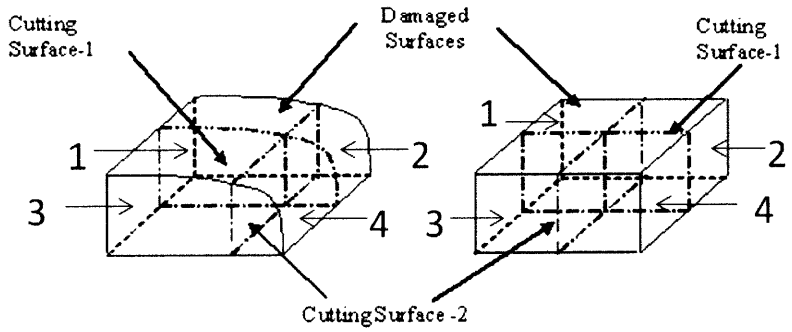

Figure 3-12: Schematic of the cutting surfaces for different tile geometries. For the microstructural analysis, sections 2 and 3 are viewed along cutting surface 1, and sections 1 and 4 are viewed along cutting surface 2. The section numbers above also correspond to the damaged tile surfaces shown in Figure 3-10, with section 1 from the top left quadrant, 2 from the top right, 3 from the bottom left, and 4 from the bottom right.

measurements were performed internally, with the tile under investigation held at vacuum within the beam line. In this configuration, an annular detector was used to record the energy of backscattered protons at a scattering angle of 165^{o}. A spectrum was also collected for a bare Mo tile for use as a baseline when interpreting the damaged tile spectra. These spectra were analyzed using SIMNRA software [28].

3.4 Microstructural Characterization

Tiles A41171I, A41258I, G20, and G13S were prepared for microstructural characterization, along with sections of the undamaged tile 070B40809R to be used for baseline comparisons. The tiles were sectioned according to Figure 3-12. The sectioned tiles were then mounted in Konductomet, a conductive hot press mounting compound available from Buehler Ltd. This compound was chosen after a comparison with several other hot press and castable mounts because it best satisfied two primary criteria, edge retention and electrical conductivity. Since the boron-TZM interface being studied is on the order of microns, good edge retention is necessary to preserve the features of interest during polishing and etching. This requires a mounting compound that adheres closely to the boundary of the sample, as any voids will allow the edge

Polishing Surface	Solution	Load (lb)/Specimen	Base Speed (rpm), Direction	Time (mm:ss)
Carbimet P400 320 Grit SiC	Water	6	200	Until Plane
UltraPol	9μm MetaDi Supreme	6	170	10:00
TexMet	3μm MetaDi Supreme	6	170	8:00
ChemoMet	0.05μm MasterMet Colloidal Silica	6	140	5:00

Table 3.3: Four step polishing procedure for tile sections using Buehler products.

to be disturbed during polishing or corroded during etching. Electrical conductivity is also important because it allows for viewing of the edge of the specimen in the SEM without charging of the mount, improving the resolution of SEM micrographs at the tile interface.

The mounted tile sections were labeled with both the tile name and a section number. For each tile, sections 1 and 4 correspond to cutting surface 2 in Figure 3-12, and sections 2 and 3 correspond to cutting surface 1. Additionally, as viewed in Figure 3-10, the section numbers correspond to the quadrant of the tile, with section 1 from the top left, 2 from the top right, 3 from the bottom left, and 4 from the bottom right. Although tile G20 is not shown, the numbering of its sections is the same as for other tiles with curved plasma facing surfaces, denoted by the prefix G.

The mounted sections of tile were mechanically polished in four steps, using a succession of progressively softer cloths and smaller particles in the polishing solutions. This procedure, using Buehler Ltd. polishing products, is given in Table 3.3. The polished samples were etched by immersion in a solution of 10% hydrogen peroxide, 20% sulfuric acid, and 70% deionized water for approximately two minutes. This etchant also stained the grains, so that microstructure was revealed optically without requiring much surface relief [29].

Optical micrographs were obtained with a 1.3 megapixel Zeiss Axiocam attached to a Zeiss DRC Stereo Microscope, capable of magnifications of 50X, 100X, 200X,

and 500X. SEM micrographs and EDX spectra were obtained with the H.H. Uhlig Corrosion Laboratory's Topcon SEM/EDX. This SEM is capable of magnifications up to 35,000X in the bottom stage used for analysis of the tile sections. Prior to SEM analysis, the tiles were etched for an additional four minutes beyond that done for optical microscopy. This was necessary to produce sufficient surface relief for good contrast between grains.

3.5 X-Ray Diffraction

XRD analysis was performed using the PANalytical X'Pert Pro and Bruker D-8 multi-purpose X-ray diffractometers at MIT's Center for Materials Science and Engineering (CMSE). This analysis was done for tiles G7 and G13S, as well as a section of the same undamaged tile used for baseline comparisons in the microstructural analysis. The PANalytical instrument has a 1.8kW sealed X-ray tube source with a copper target, and was used to collect X-ray diffraction spectra over a beam area of 10mm x 6mm for all specimens, providing a comprehensive survey of the phases present. The Bruker D-8 utilizes a similar 1.6kW sealed X-ray source with a copper target; however, this instrument also includes a Vantec 2000 2D detector, allowing for two-dimensional analysis of a circular area 0.5mm in diameter. While this lacks the comprehensive coverage of the PANalytical machine, it provides for higher resolution and an analysis of the texture or granularity of the detected phases. Given the energy of the X-ray sources in both machines, the maximum penetration depth of the X-rays is $<10\mu m$ below the boron-TZM interface for the tiles. All of the spectra collected were analyzed with accompanying GADDS software from Bruker to determine the phases present, and the results were verified against data for the suspected phases in the Inorganic Crystal Structure Database (ICSD) [30].

Chapter 4

Results

4.1 Ion Beam Analysis

4.1.1 PIGE Results

The number of counts in the 432keV boron peak and incident number of protons are presented in Table 4.1 for various areas of the six tiles, as referenced to Figure 3-10, as well as the BN block used for comparison. The counts for each area were normalized both by incident protons and counts obtained with BN, and these normalized counts were used in the simulation described in the previous chapter to determine the near surface concentrations ($\leq$30μm below the film) of boron presented here. It is interesting to note the large variation in these values. In the case of G7 in particular, large variations are even observed across the three regions surveyed.

4.1.2 RBS Spectra

RBS spectra for the five damaged tiles studied are presented in Figure 4-1. The spectrum for each tile is shown against that obtained with a bare Mo tile. The differences in energy at the RBS edge between the Mo spectrum and those of the damaged tiles are given in Table 4.2, as well as the thickness of the boron film that such a difference would indicate for a layer of pure B above the TZM substrate, as determined with SIMNRA. The spectra for G13S and G15S have far lower counting

Specimen Surface	432keV Counts	Incident Protons	B Concentration
41171, Top Center	82151	14986	0.41
41171, Center	78214	13204	0.41
41258, Top Center	91338	19393	0.36
41258, Center	87377	16933	0.37
G7, Left Center	34560	5660	0.27
G7, Center	29204	4597	0.22
G7, Right Center	202039	3647	0.37
G20, Bottom Left	1248	25684	0
G20, Top Right	88077	21257	0.32
G13S, Left Center	746853	12556	0.81
G13S, Right Center	601340	9960	0.75
G15S, Left Center	624037	9075	0.84
G15S, Right Center	574707	7495	0.79
BN	452196	12742	———

Table 4.1: PIGE data collected at various locations on the damaged tiles. The locations given are referenced to the damaged surfaces of the tiles, as viewed with the tile orientation shown in Figure 3-10. The 432keV counts in each area were normalized by both incident protons and counts obtained from BN, then used with the simulation described earlier to determine the near surface ($\leq$30μm below the film) concentrations of boron.

Tile	Energy Difference (keV)	B Film Thickness (μm)
A41171I	200	6.2
A41258I	250	7.6
G7	25	0.8
G13S	650	19.2
G15S	725	20.7

Table 4.2: The energy differences at the RBS edge between pure Mo and the damaged tiles, as well as the thickness of the B layer corresponding to such a difference, assuming a pure B film above the TZM substrate.

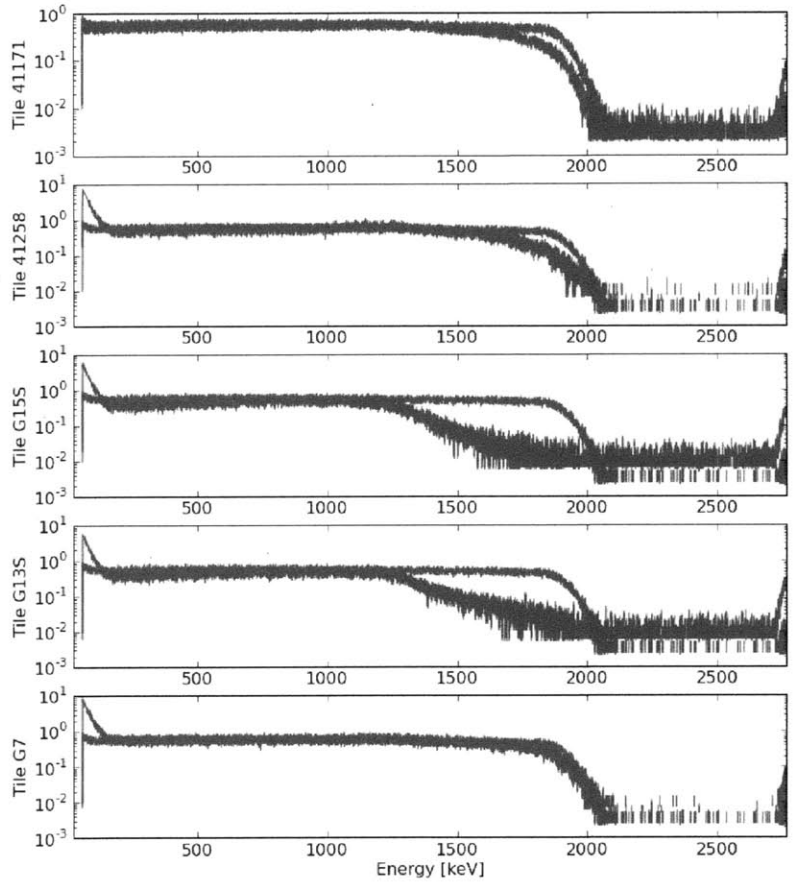

Figure 4-1: RBS spectra obtained with five of the damaged tiles, each shown against the spectrum obtained with a bare Mo tile.

rates at higher energies than the Mo tile, indicating a high concentration of boron at the tile surface; however, this counting rate decreases somewhat gradually over energy, as opposed to the steep drop that would be expected from a uniform surface layer. This seems to indicate that the boron and molybdenum are intermixed in the bumps at the surfaces of these tiles. For the two divertor tiles, A41171I and A41258I, the drop in count rate at higher energies is more pronounced, indicating that the boron film has remained largely uniform. G7, meanwhile, shows little departure from the molybdenum spectrum, and so it appears that boron has been largely depleted from the surface of this tile.

4.1.3 Integration of IBA Results

The thicknesses of the pure B layer obtained from RBS may be converted into a near surface concentration (20-30μm below the film) using the densities and molar masses of boron and molybdenum. For each tile, the pure B film thickness determined from RBS is shown in Table 4.3, along with the penetration depth of the 2MeV proton beam incident upon such a layer above the underlying Mo. The corresponding near surface concentration of B within this penetration depth is shown against the near surface B concentrations determined by PIGE in Table 4.3. In the case of the divertor tiles

Tile	B Film Thickness (μm)	Beam Penetration Depth (μm)	RBS B Conc.	PIGE B Conc.
A41171I	6.2	22.3	0.44	0.41
A41258I	7.6	23.1	0.50	0.37
G7	0.8	19.3	0.08	0.22
G13S	19.2	29.4	0.79	0.81
G15S	20.7	30.1	0.82	0.84

Table 4.3: Comparison of near surface B concentrations as determined through both PIGE and RBS.

A41171I and A41258I, the near surface boron concentration determined from RBS with an assumed film of pure boron is somewhat higher than that determined by PIGE. This indicates a film of pure boron at the surface of these tiles, along with a diffuse amount of boron in the TZM substrate. The limiter tiles G13S and G15S show the opposite, with a slightly higher concentration determined from RBS than from PIGE. Rather than a pure B film, this indicates a layer of mixed boron and molybdenum, resulting in an overall decrease in penetration of the beam versus that for a tile with a pure boron layer. This is far more pronounced for tile G7, representing a substantial amount of boron diffusion into the TZM substrate with almost no boron remaining in the original film.

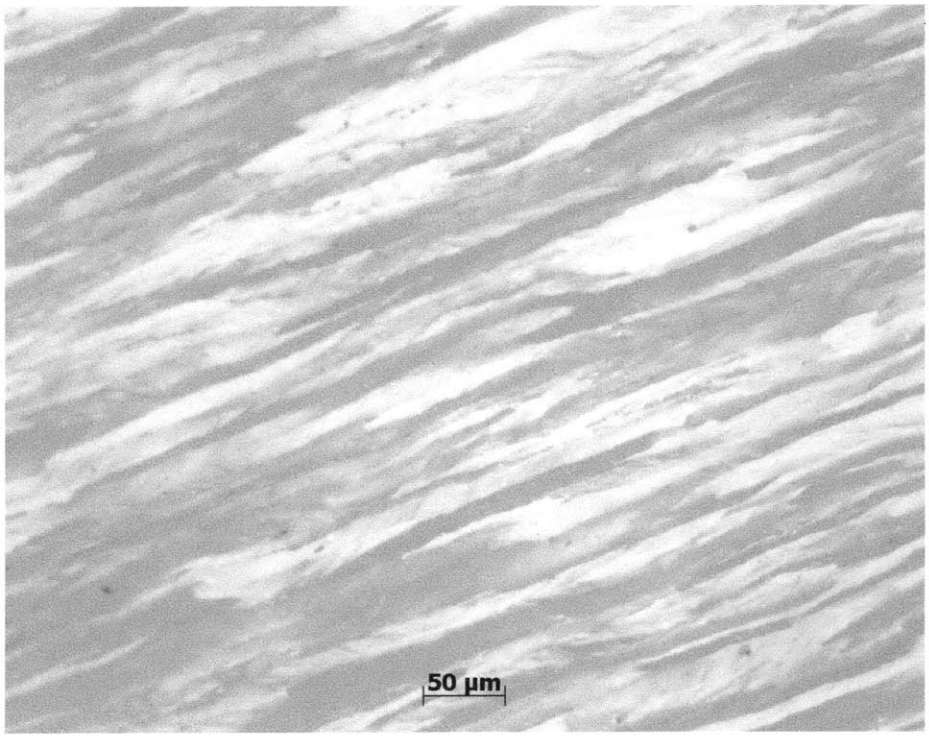

Figure 4-2: The microstructure of the undamaged TZM substrate, as viewed in a plane parallel to a side of the tile ~1mm below the boronized surface. This microstructure is dominated by elongated grains, ~20µm in width and oriented along the direction of rolling during fabrication.

4.2 Microstructural Analysis

4.2.1 Optical Micrographs

The general microstructure of the as-fabricated TZM is shown in the micrograph of the undamaged tile, presented in Figure 4-2, which shows a plane parallel to a side of the tile ~1mm below the boronized surface. This microstructure is dominated by elongated grains ~20µm wide, which are oriented lengthwise along the direction of rolling during fabrication.

The damaged tiles do not depart from this microstructure except for a few areas within about 50µm of the boron-TZM interface. At certain locations within this region, recrystallized grains were found in some of the tile sections. One such grain is shown in Figure 4-3, showing a plane parallel to a side of the tile at the boron-TZM interface in section 3 of G13S. These grains are generally observed to be 10-20µm

Figure 4-3: A recrystallized grain, ~10μm wide, found at the boron-TZM interface in section 3 of tile G13S.

in width, and oriented along the damaged surface. This is more evident in Figure 4-4, which shows a rather large recrystallized grain found in section 4 of G13S. In this case, the recrystallized grain appears to follow the surface of the indentation in the TZM, varying in width from ~10μm on one side of the defect to ~30μm on the opposite side.

A number of recrystallized grains were found in all sections of G13S, as well as sections 1, 3, and 4 of G20. The distances between these recrystallized grains varied randomly from tens of microns to several millimeters in each section, with an average areal density of approximately 30 recrystallized grains per square millimeter. There was no apparent correlation between grain location and condition of the boron film above, nor between the areal density of recrystallized grains and location on the tile surface.

The lack of more recrystallized grains is likely due to variations in the degree of cold work at the TZM surface. The TZM lattice is a body-centered cubic (BCC) structure, and as such does not have a well defined slip plane. This limits the number of slip systems for any BCC material, allowing it to retain a large amount of energy from cold work. These differences in cold work are manifest as local stresses on individual grains,

Figure 4-4: A large recrystallized grain found in section 4 of tile G13S. Note that the grain diverges from the orientation of grains in the substrate, instead wrapping around the surface defect. The width of this grain varies from ~10μm on one side of the defect to ~30μm on the opposite side.

with those grains at higher stress exhibiting a lower recrystallization temperature. These differences in local stress were likely created during swaging of the TZM rod, as well as during any subsequent machining, given the high toughness of TZM. On such short timescales (~1ms), the interaction of time at temperature, nucleation, and grain growth is highly complex, and so the extent of observed recrystallization is difficult to fully rationalize.

Interestingly, no recrystallization was found in either A41171I or A41258I. This difference between the limiter and divertor tiles may also be illustrated through the condition of the boron film as viewed in these micrographs. The boron film on section 4 of A41258I is relatively intact, as shown in Figure 4-5. The films surrounding the recrystallized grains in Figures 4-3 and 4-4, however, are highly fragmented or even absent in some locations.

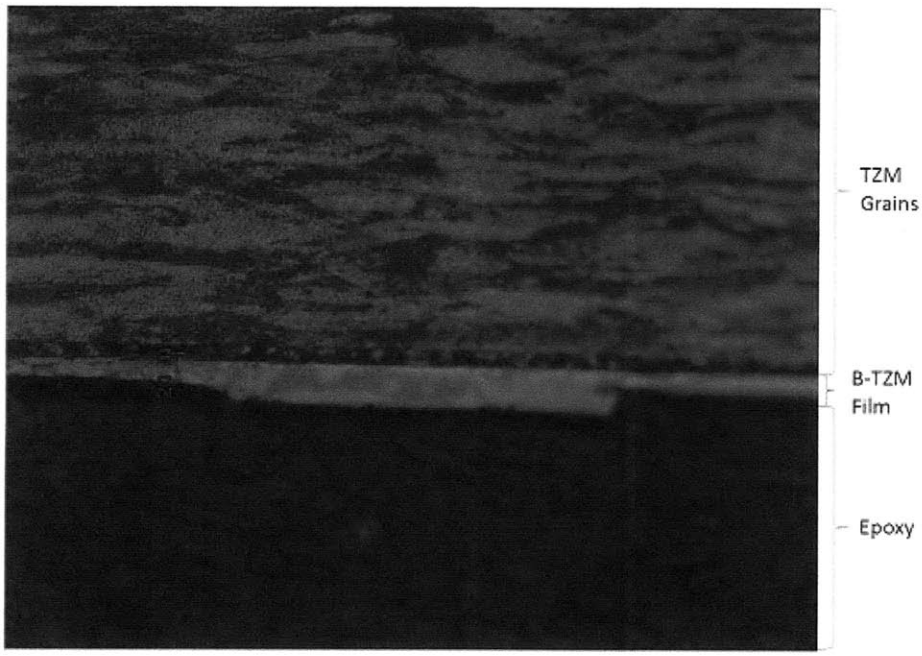

Figure 4-5: An optical micrograph of section 4 of tile A41258I, showing the relatively intact boron film.

4.2.2 SEM Micrographs

An SEM micrograph of the undamaged tile microstructure is presented in Figure 4-6, showing a plane parallel to a side of the tile ~100μm below the tile surface. This micrograph shows a TZM grain boundary with several dark pits which were most likely titanium or zirconium precipitates that were preferentially oxidized during etching. For comparison, an SEM micrograph from 100μm below the boron-TZM interface from section 2 of G13S is shown in Figure 4-7. In this micrograph, a number of precipitates are visible as small light spots arranged around the grain boundaries. The light appearance of these precipitates, as opposed to the dark pits shown in Figure 4-6, indicates that the precipitates have not been etched away and are electrically nonconductive. These properties are consistent with the intermediate boron-molybdenum phases, such as those in the phase diagram in Figure 2-4, as they are generally less reactive or electrically conductive than metals. The presence of such precipitates ~100μm below the boron film is significant, as it indicates a far greater depth of heat penetration than the ~20μm represented by recrystallization in the optical micro-

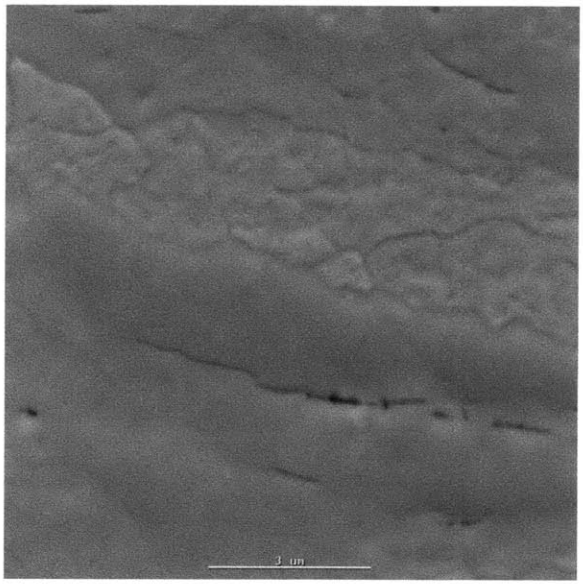

Figure 4-6: SEM micrograph of the undamaged TZM substrate along a grain boundary, showing a plane parallel to a side of the tile and approximately 100μm below the film. Note the dark pits along this boundary, which were most likely the location of Ti or Zr precipitates.

graphs. Identification of these precipitates was attempted with EDX; however, the high concentration of molybdenum prevented the detection of any other elements.

4.3 XRD Spectra

The comprehensive spectra obtained from the Panalytical X-ray diffractometer for G7 and G15S are shown in Figure 4-8, with the spectrum corresponding to G7 shown in black and that of G15S in green. The numbered lines indicate the relative intensity and twice the Bragg angle at which XRD peaks occur for molybdenum, boron, and the intermediate phases MoB, MoB_2, and Mo_2B. Better resolved but less comprehensive spectra were obtained for G7 and G15S using the Bruker D8 two-dimensional X-ray diffractometer. These spectra are presented in Figure 4-9, with the spectrum from G7 shown in green and that of G15S shown in black.

After verifying the peak locations for the intermediate phases in ICSD, it was determined that MoB_2 is present in both G7 and G15S, although in higher concentrations in G15S. MoB is also present in G15S, as well as possibly a small concentra-

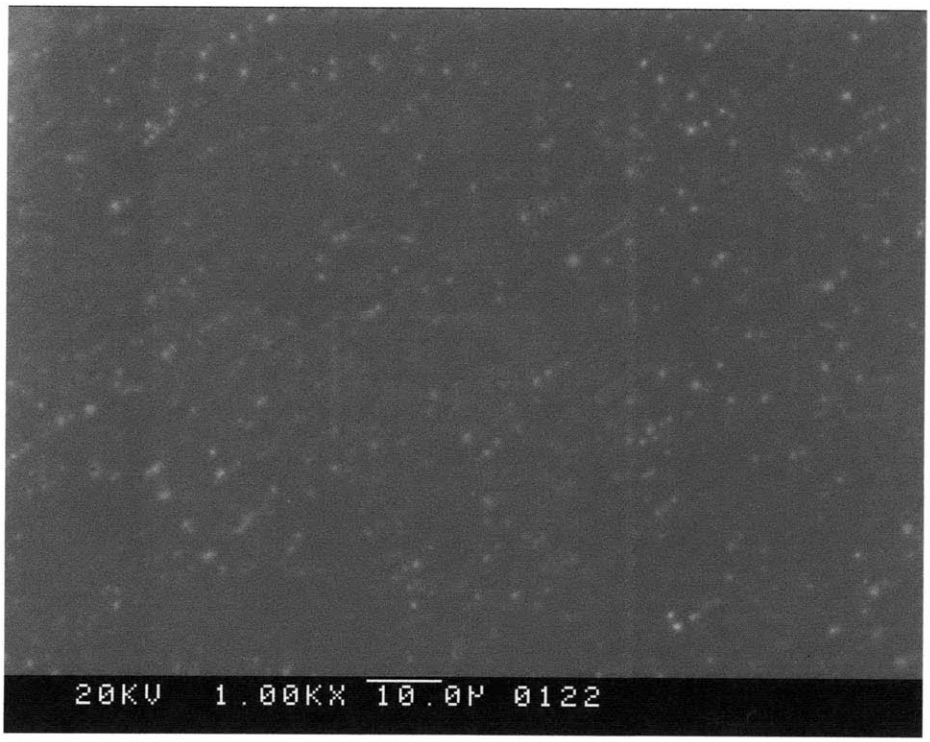

Figure 4-7: SEM micrograph of the boron-TZM interface from section 2 of tile G13S, approximately 100μm below the film. Note the light spots which indicate precipitates along the grain boundaries, possibly in the form of B-Mo phases.

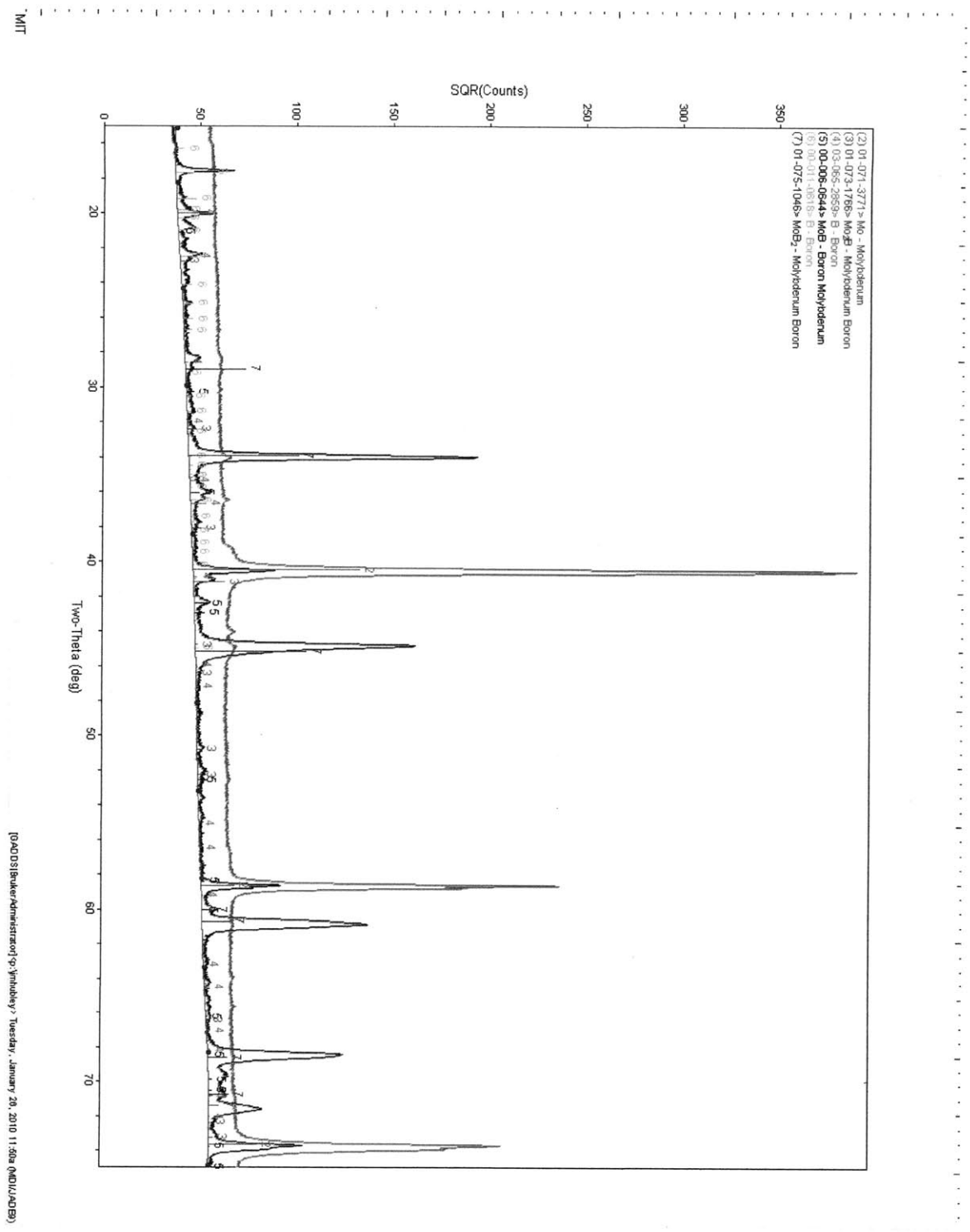

Figure 4-8: Comprehensive XRD spectra for G7 and G15S obtained with the Panalytical X-ray diffractometer, with G7 shown in green and G15S in black. The numbered lines indicate the relative intensities and 2θ values of commonly observed XRD peaks for Mo, B, and several intermediate phases.

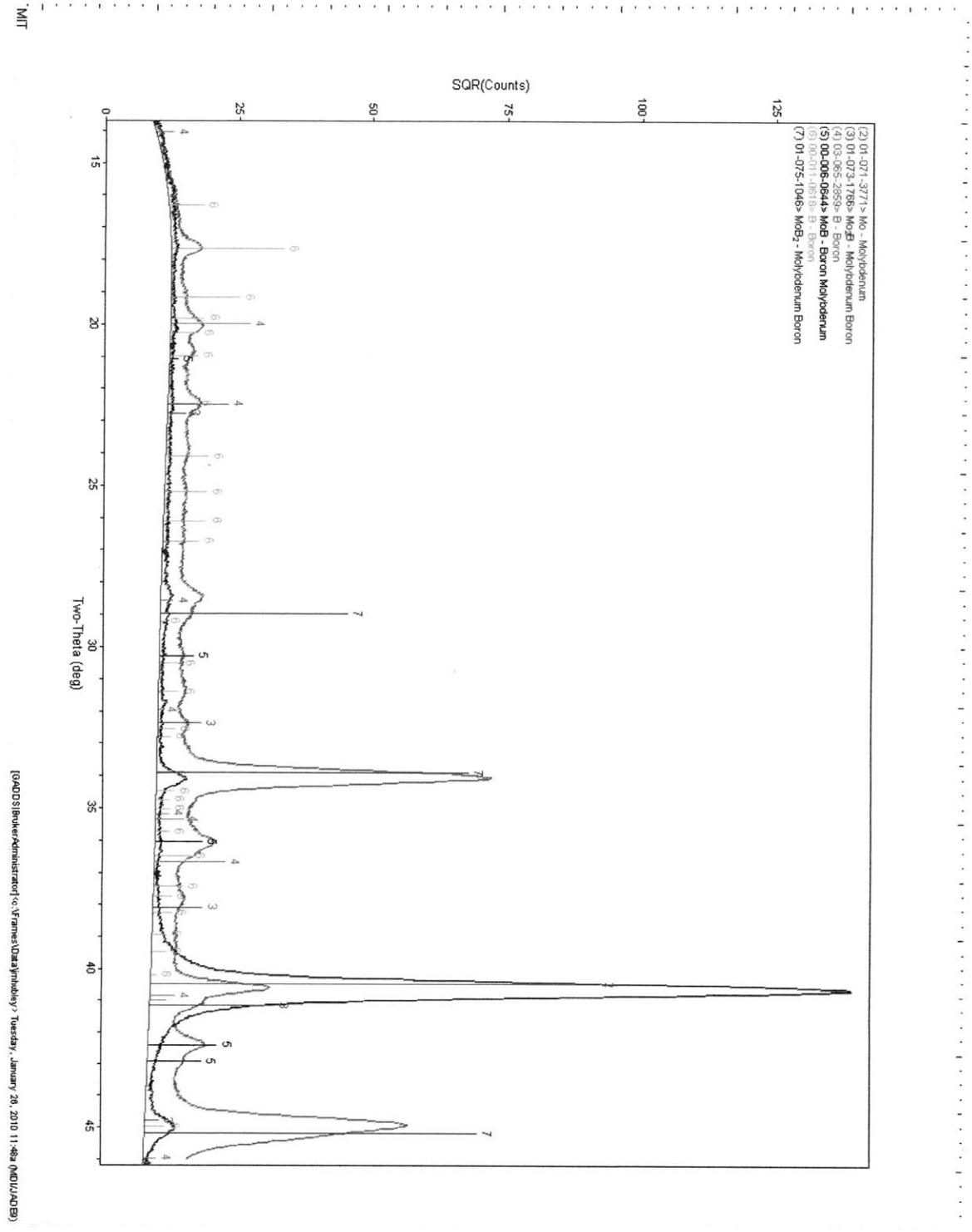

Figure 4-9: High resolution XRD spectra for G7 and G15S obtained with the Bruker D8 two-dimensional X-ray diffractometer, with G7 shown in green and G15S in black. The numbered lines indicate the relative intensities and 2θ values of commonly observed XRD peaks for Mo, B, and several intermediate phases.

tion of Mo_2B, but neither of these phases appear in G7. Similar XRD measurements were conducted on a section of the undamaged tile that was used for microstructural analysis. The Panalytical spectrum obtained for this tile is shown in black in Figure 4-10 against the spectra from G7 and G15S, shown in blue and red, respectively. The peaks of boron, molybdenum, and the intermediate phases are shown below the spectra, and the molybdenum K-β characteristic X-ray peaks are indicated to prevent misidentification as XRD peaks. Since none of the intermediate phases appear in the undamaged tile spectrum, they must be the result of temperatures reached during plasma pulses.

4.4 Summary of Tile Data

The results of the IBA, microscopy, and XRD techniques performed on the damaged tiles are summarized in Table 4.4. Together, these results present a cohesive representation of the levels of damage to PFCs in Alcator with regards to their locations within the reactor. The divertor tiles, A41171I and A41258I, show little damage beyond marked erosion of the boron film. The boron films on these tiles are quite uniform, as determined both by IBA techniques and optical micrographs.

The limiter tiles, on the other hand, present a more dramatic amount of damage. For the limiter tiles farther from the midplane, G7 and G20, a moderate amount of damage is manifest in the recrystallization and fractured film condition observed in G20, as well as the dramatic removal of the boron film from some locations of these tile surfaces. It is also interesting to note that the near surface concentration of boron changes dramatically across the surfaces of these tiles. For tile G20, greater boron depletion occurred at the flat portion of the tile surface, which extends closer toward the plasma than the rounded end at the recessed edge of the limiter module. This is not the case for G7, however, in which case the greatest boron film depletion occurred between the flat and round regions of the surface, which is not the region of the tile surface nearest to the plasma.

Nonetheless, the greatest extent of damage was observed in the limiter tiles nearer

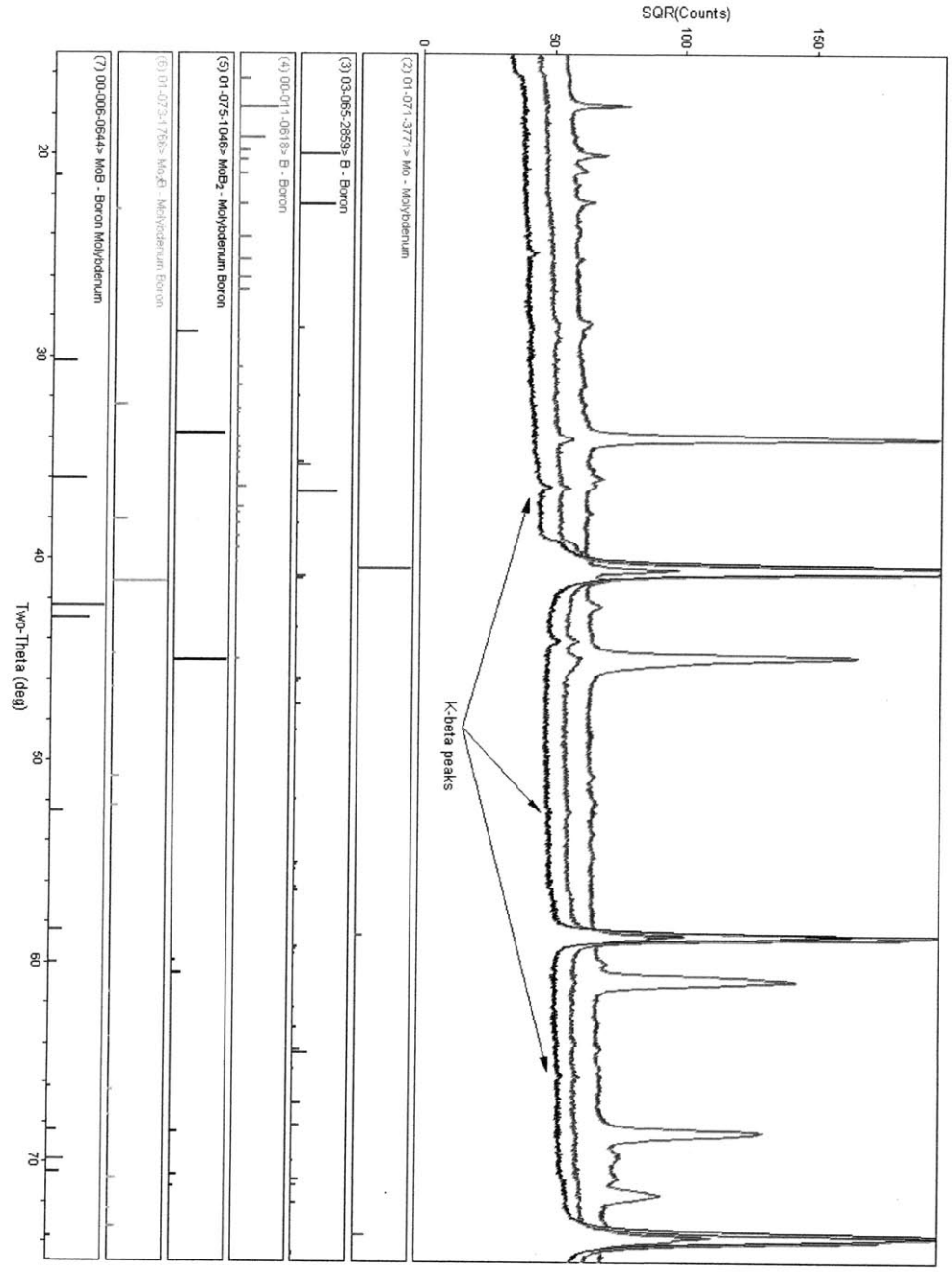

Figure 4-10: Panalytical XRD spectra for a section of undamaged tile, G7, and G15S, shown in black, blue, and red, respectively. The common XRD peaks for B, Mo, and intermediate phases are given at the bottom, and the Mo K-β peaks are indicated in the spectra.

Tile	Location (Rows Above Midplane)	Near Surface B Concentration, PIGE	Near Surface B Concentration, RBS
A41171I	Divertor Row 7	0.41	0.44
A41258I	Divertor Row 7	0.36-0.37	0.50
G7	GH Limiter Left Edge (+3)	0.22-0.37	0.08
G13S	GH Limiter Left Edge (0)	0-0.32	0.79
G15S	GH Limiter Left Edge (-1)	0.75-0.81	0.82
G20	GH Limiter Right Edge (-3)	0.79-0.84	N/A

Tile	Recrystallization	Film Condition	Thermal Interaction Depth (μm)	Intermediate Phases
A41171I	No	Uniform	N/A	N/A
A41258I	No	Uniform	N/A	N/A
G7	N/A	N/A	N/A	MoB_2
G13S	Yes	Fractured	100	N/A
G15S	N/A	N/A	N/A	MoB_2, MoB, Mo_2B
G20	Yes	Fractured	100	N/A

Table 4.4: Summary of the tile data gathered through IBA, microscopy, and XRD techniques.

to the midplane, G13S and G15S. Macroscopically, the beading at the surfaces of these tiles was far more dense and pronounced than on G7 or G20. While G13S had the same recrystallized grains as G20, G15S possessed high temperature intermediate phases of boron and molybdenum which were not found in G7. The damage to G13S and G15S was also more uniform across the surfaces of these tiles.

Chapter 5

Discussion

The IBA data present an interesting view of the boron distributions in the damaged tiles. From the PIGE analysis, it appears that the limiter tiles G13S and G15S have a significant concentration of boron at the tile surface ($\leq$30μm), while the limiter tiles G7 and G20, which are farther from the midplane, were largely depleted. The two divertor tiles, A41171I and A41258I, retained a moderate concentration of boron. When coupled with the RBS spectra, it may be seen that the boron in G13S and G15S has combined with the molybdenum in the surface bumps. The boron on the divertor tiles, however, appears to be present in a single layer above the TZM substrate. The RBS spectrum for G7 simply confirms the depletion of boron as revealed with PIGE.

The microstructural analysis of the tiles provides further information for determining the damage mechanisms present. The two divertor tiles appear to have generally intact boron films except in a few areas. These tiles also show no recrystallization or other evidence of thermal damage in the TZM substrate. G20 and G13S, on the other hand, show a large amount of damage to the boron film, as well as recrystallized grains with an average width of $\sim$20μm and an areal density of approximately 30 recrystallized grains per square millimeter. The lack of more recrystallized grains is likely due to variations in the degree of cold work at the TZM surface, manifest as local stresses on the grain boundaries, with those grains at higher stress exhibiting a lower recrystallization temperature. On such short timescales ($\sim$1ms), the interaction of time at temperature, nucleation, and grain growth is highly complex, and so

the extent of observed recrystallization is difficult to fully rationalize. SEM micrographs of these two limiter tiles also show a large number of precipitates which may be intermediate phases of boron and molybdenum to a depth below the surface of $\sim$100μm.

The exact phases present could not be determined for these tiles with EDX, but XRD performed on G7 and G15S provided useful results in this area. As determined from the XRD spectra, G15S contains a large concentration of MoB_2, as well as MoB and possibly a small amount of Mo_2B. G7, on the other hand, only shows a moderate concentration of MoB_2. As none of these phases are present in the undamaged tile, they must be the result of exposure to high temperatures during plasma pulses. The identification of such phases is of course limited to the depth of the XRD measurement, $\sim$10μm into the surface assuming a near surface concentration of boron of 0.80, the highest concentration determined by PIGE which in turn provides the greatest penetration depth. While the precipitates observed with the SEM to a depth of $\sim$100μm cannot be identified below $\leq$10μm, the prevalence of MoB_2 in the XRD region allows for a reasonable assumption that this same phase occurs at these greater depths. If this is the case, the temperature $\sim$100μm below the tile surface must reach at least 1600^{o}C to allow for the formation of this phase.

Combining these observations, the nature of the damage to these tiles may be explained fairly consistently. The lack of thermal damage evident in the divertor tiles A41171I and A41258I is consistent with an absence of transient heating. It seems likely, therefore, that the damage to the film from boronization shown for these tiles is the result of sputtering . This is reasonable, given the high fluxes of energetic deuterons in the divertor and the SRIM prediction of one sputtered boron atom for every thirteen incident deuterons at 100eV. With particle fluxes of $\sim10^{22}$particles/m^2$\cdot$s and a typical deuteron energy range of 10-100eV, the sputter erosion rate of boron in the divertor is $\sim$2-3nm/s. Over a full Alcator campaign of $\sim10^3$s, this is sufficient to erode several microns of boron without any transient events.

The situation is more complex for the tiles from the limiter. After comparing

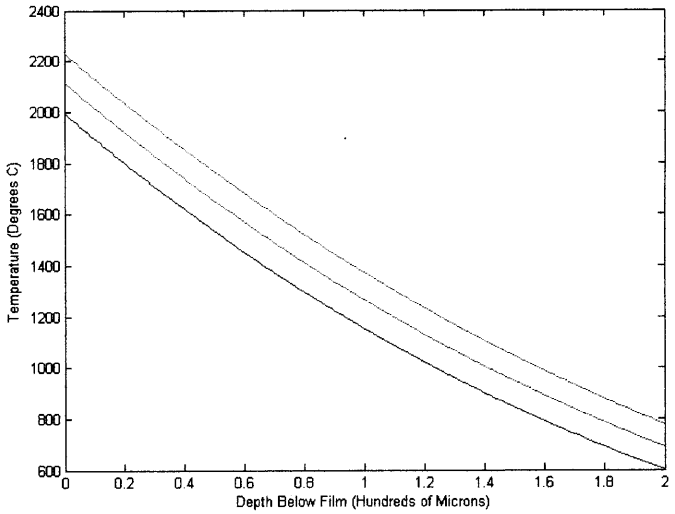

Figure 5-1: The temperature profiles throughout the limiter tiles anticipated by Equation 2.11 for a heat flux of $\sim 10^9 W/m^2$ and transient timescales of 1ms (blue), 0.9ms (red), and 0.8ms (green).

the boron-molybdenum phases detected by XRD and the boron concentrations found by PIGE to the phase diagram in Figure 2-4, the surface temperature of G7 was in the range of 2140-2375^oC, while G15S must have had a surface temperature in the range of 2140-2600^oC. Applying these surface temperature ranges to Equation 2.11 and assuming a maximum transient length of 1ms, the local heat flux at the limiter tile surface is calculated to be $\sim 10^9 W/m^2$. This heat flux may be plotted according to Equation 2.11 for several transient durations in order to approximate the temperature profile below the tile surface. The plot in Figure 5-1 shows the temperature profiles anticipated for this heat flux during transients of 1, 0.9, and 0.8ms. According to this temperature profile, a full millisecond transient is necessary to form MoB_2at $\sim 1600^oC$ up to $\sim 100\mu m$ below the tile surface; however, much shorter transients may cause recrystallization at temperatures of $\sim$ 1800^oC to a depth of $\sim 20\mu m$.

The heat flux at the tile surface may be predicted by transient behaviors of the sheath temperature and plasma density according to Equations 2.13 and 2.15. With typical values for the sheath temperature and plasma density of 5-10eV and $\leq 10^{19}$particles/m^3, the parallel heat flux is expected to be $\leq 2.5 MW/m^2$. If a transient produces an increase in both temperature and plasma density by up to one order

of magnitude each, though, this heat flux will increase to $\sim 10^8$-$10^9 W/m^2$. This is consistent with the heat flux range anticipated based upon the temperature profile and the depths of observed thermal damage.

It is also possible that this large heat flux is a result of the initial beading of the melted tile surface as it cooled. Along the magnetic field lines, the heat flux is already high during a disruption. If, in addition, the field line is normal to the side of the bead, then the typical spreading of the heat load, due to large angles between the surface normal and the field, does not occur. Rather, the bead intercepts the full parallel heat flux, leading to far higher local temperatures at the bead relative to the rest of the tile which form hot spots and accompanying recrystallization. If this were the case, the recrystallized grains that were observed would be expected to occur predominantly below beaded portions of the surface; however, there is no apparent correlation between the locations of recrystallized grains and the condition of the surface film above them. Nonetheless, this explanation cannot be excluded because the cumulative nature of the data, representing an entire Alcator campaign, allows for unrelated damage mechanisms, such as remelting and shifting of the beads.

This analysis may be applied to other tile and film systems for fusion devices, such as the beryllium coated tungsten tiles under consideration for use in the International Thermonuclear Experimental Reactor (ITER). The beryllium-tungsten phase diagram is shown in Figure 5-2 [31]. This phase diagram shows a eutectic temperature of 2100°C, which is drastically lower than the melting point of tungsten at 3422°C. In fact, for beryllium concentrations greater than 40 atomic percent, no solid phases exist above 2250°C. This is not surprising when considering the relatively low melting point of beryllium at 1287°C [32]. In this beryllium rich end of the phase diagram, several intermediate phases may be found, including Be_2W, $Be_{12}W$, and $Be_{22}W$. If the tile surfaces in ITER experience the same temperatures as those studied from the limiter in Alcator, the beryllium film will certainly melt, as well as any regions in which intermediate beryllium-tungsten phases have formed.

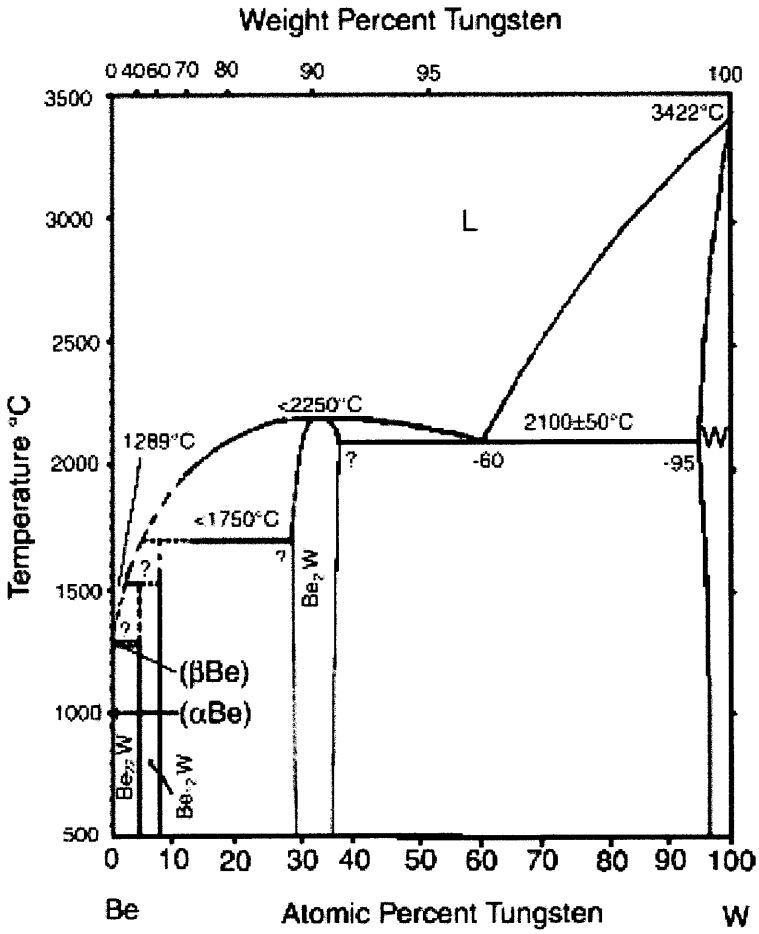

Figure 5-2: The beryllium-tungsten phase diagram.

[31]

Chapter 6

Conclusions

- The nonuniform damage encountered on boronized TZM tiles from Alcator C-Mod is the result of several distinct mechanisms.
  - For the divertor tiles, the boron film was eroded through sputtering.
    * Recrystallization was not observed, and the boron film was relatively intact on these tiles, so there is no evidence of thermal damage.
    * With fluxes of $\sim 10^{22}$particles/m^2·s and particle energies of 10-100eV, sputtering as predicted by SRIM is significant.
  - Tiles in the limiter experienced a more severe amount of damage caused primarily by thermal effects.
    * These tiles contained recrystallized grains with an average width of $\sim$20μm and an areal density of approximately one recrystallized grain for every 30 square millimeters of tile surface.
    * Additional evidence of heat penetration was found to depths of $\sim$100μm, as indicated by the precipitates found using scanning electron microscopy.
    * Various intermediate phases of boron and molybdenum were found in these tiles, some of which only form at high temperature.
    * Based upon the phases present, the temperature at the tile surfaces in the limiter was in the range 2140-2600^{o}C.

    * The extent of observed damage and estimated surface temperatures for the limiter tiles near the midplane were greater than for those limiter tiles further above or below the midplane.

- The limiter tiles experienced local heat fluxes of $\sim 10^8$-$10^9 W/m^2$, indicating a transient event on a timescale of a millisecond rather than the full $\sim$1s duration of a pulse at peak power.

  - According to the heat diffusion model, the width of the heat penetration zone and the range of surface temperatures in the limiter require a heat flux of $\sim 10^8$-$10^9 W/m^2$ over a timescale of $\sim$1ms.

  - Such a transient may result from a momentary increase by one order of magnitude in both the sheath temperature and the plasma density.

  - It is also possible that the beading which results from surface melting (and surface tension) creates, in subsequent discharges, local hot spots on the beads where the field lines intercept the bead normal to its surface. Such an enhancement of the local heat flux would then remelt at lower parallel heat fluxes in other disruptions.

  - Separating the contributions of these effects is difficult, and so further investigation is warranted to improve the understanding of plasma-tile interactions.

- This understanding of the damage mechanisms in the boronized TZM tiles from Alcator C-Mod may also be used to guide the selection of other tile and film materials for fusion reactors, such as the tungsten tiles with beryllium films under consideration for ITER.

  - As shown in the phase diagram for this system, given in Figure 5-2, the eutectic temperature of tungsten and beryllium is far lower than the actual melting point of tungsten.

- If any of the beryllium rich intermediate phases are formed at the beryllium-tungsten interface, the melting point in this region will fall to 2250^{o}C.
- Exposing these beryllium coated tungsten tiles to similar conditions as those in Alcator will lead to significant degradation as the interface continually melts and allows for the formation of intermediate phases progressively deeper into the tile.

Bibliography

[1] Jeffrey Freidberg. *Plasma Physics and Fusion Energy.* Cambridge University Press, 2007.

[2] Plasma Science and Fusion Center. http://www.psfc.mit.edu, 2010.

[3] J. Wesson. *Tokamaks.* Oxford University Press, 1987.

[4] W.J. Nuttall. Fusion as an energy source: Challenges and opportunities. Technical report, Institute of Physics, 2008.

[5] Robert Mumgaard. Alcator c-mod overview and upgrades. Gainesville, Florida, April 2009. American Nuclear Society.

[6] Peter C. Stangeby. *The Plasma Boundary of Magnetic Fusion Devices.* Institute of Physics Publishing, 2000.

[7] Harold Salvadore Barnard. External proton beam analysis of plasma facing materials for magnetic confinement fusion applications. Master's thesis, Massachusetts Institute of Technology, 2009.

[8] Kurt H. Miska, M. Semchyshen, E.P. Whelan, and Donna J. Kruzich, editors. *Physical Metallurgy and Technology of Molybdenum and Its Alloys.* AMAX Materials Research Center, 1985.

[9] John B. Lambert. Refractory metals and alloys. ASM Handbook Online, 2002.

[10] International Molybdenum Association. Molybdenum metals and alloys, 2010.

[11] B. Lipschultz, Y. Lin, D. Whyte, M.L. Reinke, A. Hubbard, I.H. Hutchinson, J. Irby, B. LaBombard, E.S. Marmar, K. Marr, J.L. Terry, S.M. Wolfe, and the Alcator C-Mod Group. Operation of alcator c-mod with high-z plasma facing components and implications. *Physics of Plasmas*, 13, 2006.

[12] R. Ochoukov, B. Lipschultz, D.G. Whyte, N. Gierse, and S. Harrison. Surface science station: a real-time diagnostic of boronization in alcator c-mod. American Physical Society-Division of Plasma Physics, November 2007.

[13] B. Lipschultz, E. Marmar, Y. Lin, D. Whyte, P. Bonoli, C. Fiore, M. Greenwald, I. Hutchinson, J. Irby, M. Reinke, J. Rice, S. Scott, J. Terry, S. Wolfe, S. Wukitch, and Alcator Team. Operation of alcator c-mod with high-z plasma facing components with and without boronization. In *33rd EPS Conference on Plasma Physics*, Rome, June 2006.

[14] Thomas E. Tietz and Jess W. Wilson. *Behavior and Properties of Refractory Metals.* Stanford University Press, 1965.

[15] Plansee. *TZM Quality Assurance Documentation Service.* Plansee, 1991.

[16] Gao Yang, Hei Zu-kun, Xu Xiaolei, and Xin Gang. Formation of molybdenum boride cermet coating by the detonation spray process. *Journal of Thermal Spray Technology*, 10:456–460, 2000.

[17] J.P. Hirvonen. *Handbook of Modern Ion Beam Materials Analysis.* Materials Research Society, 1995.

[18] Robert B. Day and Torben Huus. Gamma radiation from b-10 bombarded by protons. *Physical Review*, 95(4), August 1954.

[19] Wei-Kan Chu. Rutherford backscattering spectrometry. ASM Handbook Online, 2002.

[20] Glenn F. Knoll. *Radiation Detection and Measurement.* John Wiley & Sons, Inc., third edition edition, 2000.

[21] Robert E. Reed-Hill and Reza Abbaschian. *Physical Metallurgy Principles.* PWS Publishing Company, third edition edition, 1994.

[22] B.D. Cullity. *Elements of X-Ray Diffraction.* Addison-Wesley Publishing Company, Inc., second edition edition, 1978.

[23] Neil E. Todreas and Mujid S. Kazimi. *Nuclear Systems I: Thermal Hydraulic Fundamentals.* Taylor & Francis Group, 1990.

[24] H.S. Carslaw and J.C. Jaeger. *Conduction of Heat in Solids.* Clarendon Press, 1986.

[25] Rainer Behrisch. Evaporation for heat pulses on ni, mo, w and atj graphite as first wall materials. *Journal of Nuclear Materials*, 93 & 94:498–504, 1980.

[26] G.V. Samsonov. *Handbook of Refractory Compounds.* IFI/Plenum, 1980.

[27] J.F. Ziegler, M.D. Ziegler, and J.P. Biersack. The stopping and range of ions in matter, 2008.

[28] Matej Mayer. Simnra, 2009.

[29] Buehler Ltd. Technical Information. Molybdenum alloys, 2009.

[30] Inorganic Crystal Structure Database. Powder diffraction file, 2010.

[31] R.P. Doerner, M.J. Baldwin, and R.A. Causey. Beryllium-tungsten mixed-material interactions. *Journal of Nuclear Materials*, 342:63–67, 2005.

[32] CRCnetBASE. Handbook of chemistry and physics, 2010.